Suprathermal electrons from the anti-Stokes Langmuir decay instability cascade

Q. S. Feng ⦿,[1] R. Aboushelbaya,[1] M. W. von der Leyen,[1] B. T. Spiers,[1] R. W. Paddock,[1] I. Ouatu,[1] R. Timmis,[1]
R. H. W. Wang,[1] L. H. Cao,[2,3,*] Z. J. Liu,[2,3] C. Y. Zheng,[2,3] X. T. He,[2,3] and P. A. Norreys[1,4,†]

[1]*Department of Physics, Atomic and Laser Physics sub-Department, University of Oxford, Clarendon Laboratory,*
Oxford OX1 3PU, United Kingdom
[2]*Institute of Applied Physics and Computational Mathematics, Beijing 100094, China*
[3]*HEDPS, Center for Applied Physics and Technology, Peking University, Beijing 100871, China*
[4]*John Adams Institute, Denys Wilkinson Building, Oxford OX1 3RH, United Kingdom*

The study of parametric instabilities has played a crucial role in understanding energy transfer to plasma and, with that, the development of key applications such as inertial confinement fusion. When the densities are between $0.11n_c \lesssim n_e \lesssim 0.14n_c$ and the electron temperature is in inertial confinement fusion-relevant temperatures, anomalous hot electrons with kinetic energies above 100 keV are generated. Here a new electron acceleration mechanism—the anti-Stokes Langmuir decay instability cascade of forward stimulated Raman scattering—is investigated. This mechanism potentially explains anomalous energetic electron generation in indirectly driven inertial confinement fusion experiments, it also provides a new way of accelerating electrons to higher energy for applications such as novel x-ray sources.

I. INTRODUCTION

Stimulated Raman scattering (SRS) [1] is a three-wave interaction process where an incident light decays into a forward-propagating Langmuir wave and either a backward-scattered (backward-SRS) or a forward-scattered (forward-SRS) electromagnetic wave. Backward-SRS leads to a large energy loss of the incident laser energy in indirect-drive [2,3] and hybrid-drive inertial confinement fusion (ICF) [4,5]. The hot electrons generated by the trapping and breaking of SRS-induced Langmuir waves preheat the fusion fuel, while energy losses on the inner cones of beams on the National Ignition Facility may have a detrimental effect on the symmetrical. compression of fusion capsule, albeit partially compensated by the cross-beam energy transfer process. For these reasons, SRS and hot electron generation should be suppressed to as low a level as possible for indirect-drive.

Many particular smoothing techniques are applied to suppressing SRS and stimulated Brillouin scattering (SBS), including smoothing by spectral dispersion (SSD) [6] and polarization smoothing (PS) [7].

The processes responsible for this suprathermal electron generation are still not completely understood. The energy of electrons generated from the backward-SRS is much lower than 100 keV [8]. Possible mechanisms that have been studied to date. include SRS rescatterings, corresponding Langmuir decay instability (LDI) [9,10] and the two-plasmon decay instability [11,12]. Other authors [13–16] have investigated the electrons accelerated by the forward-SRS-induced Langmuir waves.

We draw the attention of the reader to the very elegant work of Winjum *et al.* [17] who showed that 100 keV electrons are generated through SRS rescattering processes, such as backward-SRS of backward-SRS, backward-SRS of forward-SRS, and the corresponding Langmuir decay instability of the rescattering processes when the electron density $n_e \leqslant 0.1n_c$.

We build on these fascinating insights by showing here that when $T_e = 2.5$ keV, and $n_e \gtrsim 0.1n_c$, backward-SRS of backward-SRS is not allowed. Similarly, for $n_e \gtrsim 0.108n_c$, backward-SRS of forward-SRS is forbidden, since the three-wave matching conditions of rescatterings are not satisfied. Instead, in the region of $n_e \gtrsim 0.108n_c$, evidence is provided that the anomalous hot electrons with energy above 100 keV could possibly arise from anti-Stokes Langmuir decay instability (denoted as anti-Stokes LDI or ALDI) cascade of forward-SRS. It provides a potential explanation for the higher-energy electrons generation in earlier National Ignition Facility (NIF) experiments, in which such high gas-fill densities are used [18].

The various wave-wave processes discussed in this article are quite numerous and we have therefore tried to avoid the use of acronyms in the text wherever possible. For clarity, a schematic of the dispersion relationships of the wave-wave processes discussed in this paper is provided in Fig. 1.

In indirect drive [2,3,19] or hybrid drive inertial confinement fusion [4,5], suprathermal electrons preheat the fusion fuel, either by direct propagation into the fuel capsule itself or by the secondary generation of hard x rays that arise when hot electrons propagate into the *Hohlraum* walls or surrounding plasma [20,21]. On the other hand, in fast ignition [22], the fusion fuel is ignited by collisional stopping of suprathermal electrons that propagate from the critical density to the high-density hot spot on the side of the compressed fusion fuel. Therefore, suprathermal electrons generated by
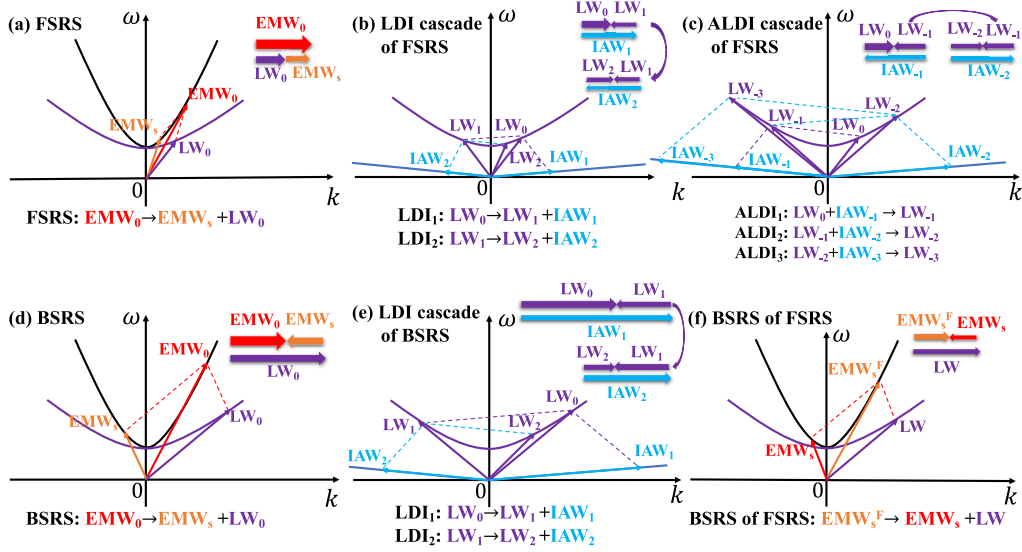
FIG. 1. Schematic diagram of (a) forward-SRS (FSRS), (b) LDI cascade of forward-SRS, (c) ALDI cascade of forward-SRS, (d) backward-SRS (BSRS), (e) Langmuir decay instability cascade of backward-SRS, and (f) backward-SRS of forward-SRS. For completeness, EMW is the electromagnetic wave, LW is the Langmuir wave, and IAW is the ion acoustic wave.

the two-stage acceleration mechanism of backward-SRS and forward-SRS in this article might have advantageous effects for inertial fusion by enabling fast ignition using plasma optics and beam-combiners [23,24] at lower intensities than previously thought possible. Similarly, the novel mechanism of electron acceleration by anti-Stokes and Stokes Langmuir decay instability cascade of forward-SRS might be a promising mechanism to generate higher-energy electrons for radiography purposes [25,26], complementing those generated with the use of petawatt-class laser pulses.

In this work, we first set the stage by elucidating the parameter regime for the convective and absolute instability of backward-SRS and forward-SRS that is provided by linear theory. Following that, the relevant wave-breaking and particle-trapping model is discussed. This model describes the two-stage electron acceleration by backward-SRS and forward-SRS. It is then shown that electrons trapped by the backward-SRS-induced Langmuir wave are also trapped and accelerated by the forward-SRS-induced Langmuir wave directly in the higher-electron-density regions where no rescatterings exist as intermediate processes.

We concentrate on three regions. When $n_e \lesssim 0.108 n_c$ (Region I), backward-SRS, backward-SRS of forward-SRS and Langmuir decay instability accelerate electrons to high energy. Only when $0.108 n_c \lesssim n_e \lesssim 0.138 n_c$ (Region II) are electrons prevented from being accelerated by rescattering and by forward-SRS. However, in Region II, anomalous hot electrons with energies above 100 keV are also generated, which is due to the Langmuir wave having a higher phase velocity than the backward-SRS-induced Langmuir wave. It is demonstrated that this higher phase velocity Langmuir wave is due to the generation of anti-Stokes Langmuir decay instability in a cascade associated with forward-SRS. When $n_e \gtrsim 0.138 n_c$ (Region III), the electrons are first trapped by the backward-SRS-induced Langmuir waves and will be

accelerated by the resonance and trapping mechanisms. And then the electrons accelerated by the backward-SRS-induced Langmuir waves will be further trapped and accelerated by the forward-SRS-induced Langmuir waves directly. If the wave-breaking threshold of electron trapping by forward-SRS is reached, then the energetic electrons with maximum momenta will be generated. In this way, the two-stage electron acceleration process by backward-SRS and forward-SRS is allowed. The electron temperature has little effect on the electron acceleration mechanisms, while the decisive factor is the electron density. Last, within the range $0.1 n_c \leqslant n_e \leqslant 0.2 n_c$, electron density region with $0.108 n_c \lesssim n_e \lesssim 0.138 n_c$ is shown as a better choice to reduce the suprathermal electron population to a low level.

This paper is arranged as follows. In Sec. II, linear theory is used to describe the convective and absolute instability regions of the backward-SRS and forward-SRS processes. The wave-breaking maximum electric field amplitude, which provides insight into the precise conditions required for the two-stage electron acceleration by both backward-SRS and forward-SRS, is also discussed. In Sec. III, a full-relativistic kinetic Vlasov-Maxwell code is used to (a) simulate the electron cascade acceleration by backward-SRS and forward-SRS in Region III, (b) study the anti-Stokes Langmuir decay instability cascade of forward-SRS in Region II, and (c) understand the rescattering processes in Region I. In Sec. IV, it is shown that both one-dimensional (1D) and three-dimensional fully relativistic kinetic particle-in-cell simulations give similar results to those obtained from Vlasov-Maxwell simulations, confirming that the results are independent of the chosen computational platform and are therefore robust. In Sec. V, the effects of both the electron temperature and inhomogeneous plasma conditions on electron acceleration are discussed. Section VI then summarizes and concludes the paper, along with an outline of future research directions.

TABLE I. The Langmuir wave wave number k_L, electron momentum p_ϕ, and kinetic energy E_ϕ at the Langmuir wave phase velocities of the different instabilities. The minus signs of k_L and p_ϕ represent waves propagating in the negative direction. The initial electron temperature is $T_e = 2.5\,\text{keV}$.

	FSRS			LDI1 of FSRS		LDI2 of FSRS		ALDI1 of FSRS		ALDI2 of FSRS		ALDI3 of FSRS	
n_e	k_L	p_ϕ	E_ϕ	k_L	p_ϕ	k_L	p_ϕ	k_L	p_ϕ	k_L	p_ϕ	k_L	p_ϕ
(n_c)	$(\lambda_{\text{De}}^{-1})$	$(m_e c)$	(keV)	$(\lambda_{\text{De}}^{-1})$	$(m_e c)$	$(\lambda_{\text{De}}^{-1})$	$(m_e c)$	$(\lambda_{\text{De}}^{-1})$	$(m_e c)$	$(\lambda_{\text{De}}^{-1})$	$(m_e c)$	$(\lambda_{\text{De}}^{-1})$	$(m_e c)$
0.1	0.076	2.4	818	−0.061	−∞	0.045	+∞	−0.092	−1.21	0.108	0.88	−0.123	−0.71
0.12	0.078	2.09	672	−0.063	−∞	0.047	+∞	−0.094	−1.15	0.109	0.86	−0.125	−0.70
0.2	0.091	1.25	309	−0.075	−∞	0.059	+∞	−0.106	−0.90	0.122	0.73	−0.137	−0.61

	BSRS			LDI1 of BSRS		LDI2 of BSRS		BSRS of FSRS		LDI1 of BSRS of FSRS		LDI2 of BSRS of FSRS	
n_e	k_L	p_ϕ	E_ϕ	k_L	p_ϕ	k_L	p_ϕ	k_L	p_ϕ	k_L	p_ϕ	k_L	p_ϕ
(n_c)	$(\lambda_{\text{De}}^{-1})$	$(m_e c)$	(keV)	$(\lambda_{\text{De}}^{-1})$	$(m_e c)$	$(\lambda_{\text{De}}^{-1})$	$(m_e c)$	$(\lambda_{\text{De}}^{-1})$	$(m_e c)$	$(\lambda_{\text{De}}^{-1})$	$(m_e c)$	$(\lambda_{\text{De}}^{-1})$	$(m_e c)$
0.1	0.33	0.25	16					0.167	0.48	−0.152	−0.54	0.136	0.62
0.12	0.29	0.28	20										
0.2	0.18	0.43	46	−0.169	−0.48	0.153	0.54						

II. THEORETICAL ANALYSIS

All of the instabilities (backward-SRS, forward-SRS, the various rescattering processes, as well as the Stokes/anti-Stokes Langmuir decay instability cascades from backward-SRS/forward-SRS) satisfy the three-wave matching conditions resulting from the laws of energy and momentum conservation. By combining the three-wave matching conditions with the dispersion relations of electromagnetic waves, Langmuir waves (LW), and ion-acoustic waves (IAW), it is possible to calculate the wave number k_L, the electron momentum p_ϕ, and the kinetic energy E_ϕ associated with the Langmuir wave phase velocities of the different instabilities, as shown in Table I.

When the wave number of the Langmuir wave satisfies $k_L \lambda_{\text{De}} < 0.29$ (λ_{De} is the electron Debye length), both the Langmuir decay instability cascade and the anti-Stokes Langmuir decay instability cascade occur more easily and so are characterized by being in the nonlinear wave-wave regime or fluid regime. On the other hand, when $k_L \lambda_{\text{De}} \geqslant 0.29$, a frequency-broadened spectrum is observed. This spectrum is associated with electron trapping, which places this in the nonlinear wave-particle, or kinetic, regime [27,28].

As shown in Table I, three typical electron densities were used in this paper to understand the mechanisms of electron acceleration. First, when $n_e = 0.1 n_c$, the wave number of the backward-SRS-induced Langmuir wave is $k_L^B \lambda_{\text{De}} = 0.33 \geqslant 0.29$. Thus, the Langmuir decay instability cascade of backward-SRS is not allowed, which is the same as the case when $n_e = 0.12 n_c$. However, the rescattering of forward-SRS by backward-SRS is allowed. The wave number of rescattering-induced Langmuir wave is $k_L \lambda_{\text{De}} = 0.167 < 0.29$. The Langmuir decay instability cascade of this rescattering is also allowed (not shown in Table I).

Second, when $n_e = 0.12 n_c$ and $n_e = 0.2 n_c$, rescattering of forward-SRS by backward-SRS is not allowed because the three wave matching condition of this rescattering process is not satisfied. However, the Langmuir decay instability cascade of backward-SRS is allowed when $n_e = 0.2 n_c$ because the

wave number of the backward-SRS-induced Langmuir wave is $k_L^B \lambda_{\text{De}} = 0.18 < 0.29$.

Third, when $n_e = 0.1$, 0.12, and $0.2 n_c$, the wave number of the forward-SRS-induced Langmuir wave is $k_L^F \lambda_{\text{De}} = [0.076, 0.078, 0.091] < 0.29$. This means that both the Langmuir decay instability and the anti-Stokes Langmuir decay instability of forward-SRS are allowed.

From the three-wave equations [29–31], the theoretical growth rate of SRS scattered light in homogeneous plasmas is [1,32]

$$\gamma_{tR} = \left[\frac{2\gamma_{0R}}{\sqrt{|v_{gs}|v_{gL}}} - \left(\frac{v_s}{|v_{gs}|} + \frac{v_L}{v_{gL}} \right) \right] \cdot \frac{|v_{gs}|v_{gL}}{|v_{gs}| + v_{gL}}, \quad (1)$$

where

$$\gamma_{0R} = \frac{1}{4}\sqrt{\frac{\omega_{pe}^2}{\omega_s \omega_L}} k_L a_0 \quad (2)$$

is the maximum temporal growth rate of SRS [33,34]. $a_0 = eE_0/m_e\omega_0$ and $\omega_{pe} = \sqrt{4\pi n_e e^2/m_e}$ are the electron quiver velocity and the electron plasma frequency, respectively. In addition, v_i, v_{gi}, ω_i are the damping rates, group velocities, and frequencies of the SRS scattered light ($i = s$) and the Langmuir wave ($i = L$). The damping rate of the backscattered light v_s is negligible since it is much lower than the Landau damping v_L of the Langmuir wave, i.e., $v_s = 0$. The collisions of the forward-SRS are neglected for simplicity. When $2\gamma_{0R}/\sqrt{|v_{gs}|v_{gL}} > v_L/v_{gL}$, i.e., $\gamma_{tR} > 0$, SRS is in the absolute instability regime. However, when $2\gamma_{0R}/\sqrt{|v_{gs}|v_{gL}} < v_L/v_{gL}$, i.e., $\gamma_{tR} < 0$, SRS is in the convective instability regime. The gain of SRS is

$$G_R = 2\frac{\gamma_{0R}^2}{v_L v_{gs}} L = \frac{1}{8}\frac{k_L^2 a_0^2 \omega_{pe}^2}{v_L v_{gs}\omega_s\omega_L}L, \quad (3)$$

where L is the homogeneous plasma length.

The above linear theory is dealing with a Maxwellian plasma, which decides the initial state of the instabilities. Much of that analysis is not valid as soon as particles begin to be trapped. After the plasma wave amplitude becomes
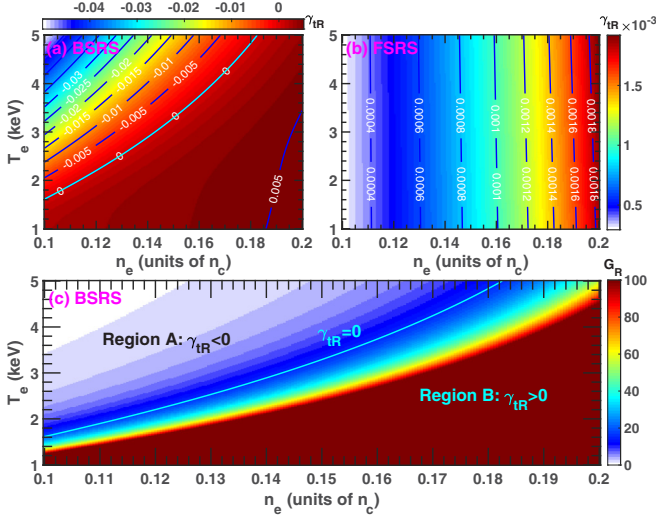
FIG. 2. The variation of (a) backward-SRS theoretical growth rate, (b) forward-SRS theoretical growth rate, and (c) backward-SRS gain with the electron density and the electron temperature. The incident laser intensity is $I_0 = 1 \times 10^{16}$ W/cm^2 and the plasma length is $L = 400c/\omega_0$.

large, the Landau damping of the Langmuir wave decreases to nearly zero due to particle trapping. Thus, the SRS becomes absolute and the gains of both backward and forward SRS are different from their linear values. Therefore, the linear analyses can give an initial estimation of the growth rates and gains of the instabilities, which will decide the strength of Langmuir wave induced by instabilities, thus determining the source of ultra-high-energy electron production.

Figure 2(a) shows that in the high-electron-temperature and low-electron-density region (i.e., where $\gamma_{tR} < 0$) the backward-SRS is in the convective instability regime. At the same time, in the low-electron-temperature and high-electron-density region (i.e., where $\gamma_{tR} > 0$) the backward-SRS is in the absolute instability regime.

Figure 2(b) shows the forward-SRS growth rate. Because absolute instability is only possible for oppositely propagating daughter waves [35], forward-SRS in homogeneous media is never absolutely unstable. The collision damping of forward-SRS may dominate (which is included in our particle-in-cell simulations in Sec. IV). However, the growth rate of the forward-SRS is lower than that of backward-SRS in higher electron density regions.

The contour pictures of backward-SRS gain are shown in Fig. 2(c). Since the wave number of the backward-SRS-induced Langmuir wave is small in the high-electron-density or low-electron-temperature region, the Landau damping of backward-SRS-induced Langmuir wave is very low. Thus, the backward-SRS gain is very large. When $I_0 = 1 \times 10^{16}$ W/cm^2, $L = 400c/\omega_0$, and $\gamma_{tR} = 0$, the backward-SRS gain is $G_R \simeq 16$.

Region A in Fig. 2(c) is the convective backward-SRS instability region, where $\gamma_{tR} < 0$ and $G_R \lesssim 16$. Region B is the absolute backward-SRS instability region, where $\gamma_{tR} > 0$ and $G_R \gtrsim 16$. If the electron temperature is fixed at $T_e = 2.5$ keV, then the backward-SRS gain $G_R = 3.4$ is very low when $n_e =$

$0.1n_c$, but on the other hand $G_R = 2.1 \times 10^4 \to \infty$ is very high when $n_e = 0.2n_c$. When $\gamma_{tR} = 0$, the transition between the convective to absolute backward-SRS instability regimes is $n_e \simeq 0.128n_c$. If the electron density is fixed at $n_e = 0.2n_c$, then backward-SRS is an absolute instability and the gain is very high when the electron temperature lies between $T_e \in [1, 5]$ keV.

The kinetic energy of electrons at the Langmuir wave phase velocity is $E_\phi = m_e v_\phi^2/2$ and $E_\phi = (\gamma_\phi - 1)m_e c^2$ in nonrelativistic and relativistic plasmas, respectively, where $\gamma_\phi = 1/\sqrt{1 - (v_\phi/c)^2}$ is the Lorentz factor and v_ϕ is the Langmuir wave's phase velocity. This means that when $T_e = 2.5$ keV, $n_e = 0.2n_c$, the phase velocity of backward-SRS $v_\phi^B = 0.398c$ is on the borderline of the relativistic threshold and the effects of relativity are not immediately obvious. On the other hand, the phase velocity of forward-SRS $v_\phi^F = 0.782c$ is much larger than that of backward-SRS, which means that the relativistic effect of electrons with the forward-SRS-induced Langmuir wave phase velocity is more obvious. The corresponding kinetic energy of electrons is $E_\phi^B = 46$ keV and $E_\phi^F = 310$ keV for the backward-SRS and forward-SRS-induced Langmuir wave phase velocities, respectively. The maximum or minimum velocity of electrons that are accelerated by the Langmuir wave is related to its phase velocity, i.e., $v_{max} = v_\phi + v_{tr} = v_\phi + 2\sqrt{eE_{max}/(m_e k)}$ and $v_{min} = v_\phi - v_{tr} = v_\phi - 2\sqrt{eE_{max}/(m_e k)}$.

Since the finite electron temperature has to be included explicitly, a warm wave breaking model must be used [36]. In the limit of slow phase velocity waves, $v_{te} \ll v_\phi \ll c$ [37], a warm nonrelativistic wave breaking field E_{max} has been calculated using the warm fluid model by Coffey [38]. In the ultrarelativistic phase velocity $v_\phi/c = 1$ limits, the warm relativistic wave breaking fields given by Katsouleas and Mori [39] and by Trines and Norreys [40] are valid. The warm relativistic wave breaking field is valid for $\gamma_\phi v_{te} \gg 1$. In the parameter space of this work, $T_e = 2.5$ keV, when the electron density n_e varies from $0.1n_c$ to $0.2n_c$, the phase velocity of the backward-SRS-induced Langmuir waves v_ϕ^B varies from $0.24c$ to $0.40c$, while that of forward-SRS v_ϕ^F varies from $0.92c$ to $0.78c$. Therefore, $v_{te} \ll v_\phi^B \ll c$, $v_{te} \ll v_\phi^F < c$ satisfies the warm nonrelativistic wave-breaking conditions. Although the phase velocity of the forward-SRS-induced Langmuir wave is large, it is also lower than c, i.e., $v_\phi^F/c \neq 1$. Also $\gamma_\phi \cdot v_{te}/c \in [0.18, 0.11] \ll 1$ when $n_e \in [0.1, 0.2]n_c$. For these reasons, the warm fully relativistic wave breaking limits are not valid for the parameter space explored in the current work. Thus, the maximum electric field of the Langmuir wave is calculated by Coffey's warm nonrelativistic wave breaking limit [36,38],

$$E_{max} = \frac{m_e v_\phi \omega_{pe}}{e} \sqrt{1 + 2\beta^{1/2} - \frac{8}{3}\beta^{1/4} - \frac{1}{3}\beta}, \quad (4)$$

where $\beta = 3v_{te}^2/v_\phi^2$ and ω_{pe}, v_{te} are the plasma frequency and the electron thermal velocity. In addition, it is possible to calculate the wave number of the Langmuir wave from the Langmuir wave dispersion relation:

$$k \simeq \frac{1}{\lambda_{De}} \sqrt{\frac{v_{te}^2}{v_\phi^2 - 3v_{te}^2}} = \frac{1}{\lambda_{De}} \sqrt{\frac{\beta}{3 - 3\beta}}. \quad (5)$$
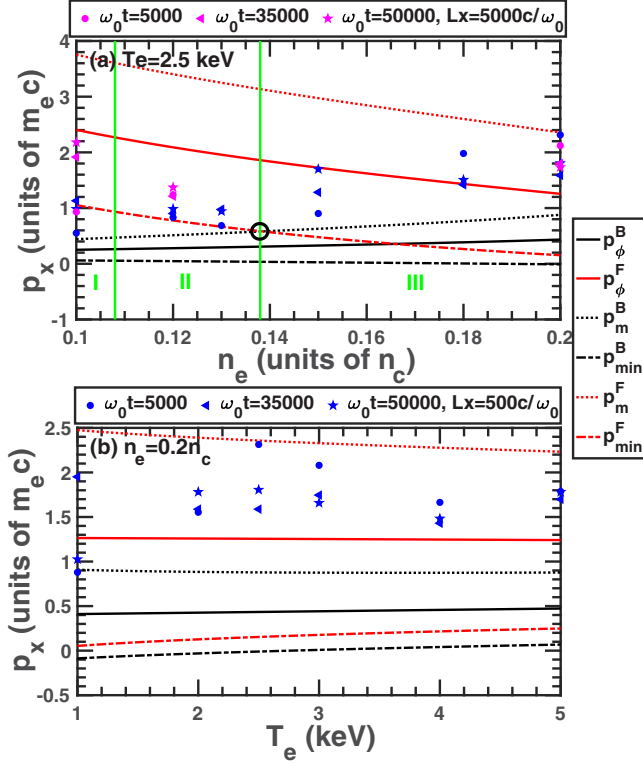
FIG. 3. The variation of p_x with (a) electron density n_e when $T_e = 2.5$ keV and (b) electron temperature T_e when $n_e = 0.2 n_c$. The Vlasov simulation data points of the maximum electron momenta are chosen at $\omega_0 t = 5000$ (circle), $\omega_0 t = 35\,000$ (triangle), and $\omega_0 t = 50\,000$ (pentacle). The simulation data points plotted in pink are in the condition for $I_0 = 3 \times 10^{15}$ W/cm^2, $L_x = 5000 c/\omega_0$ (shown in Sec. III B). The simulation data points plotted in blue are in the condition for $I_0 = 1 \times 10^{16}$ W/cm^2, $L_x = 500 c/\omega_0$, except that the simulation data points when $T_e = 2.5$ keV, $n_e = 0.1 n_c$ are in the condition for $I_0 = 5 \times 10^{16}$ W/cm^2 (shown in Sec. III A). The lines are from theoretical model and the points are from Vlasov simulations. p_m^B and p_m^F represent the maximum momenta calculated from the wave-breaking maximum electric field of the backward-SRS-induced Langmuir wave ($p_{\max}^B$) and the forward-SRS-induced Langmuir wave ($p_{\max}^F$).

Thus the maximum momentum is $p_{\max} = \gamma_{\max} m_e v_{\max}$ and the maximum kinetic energy is $E_m = (\gamma_{\max} - 1) m_e c^2$. The relationship between the electron momentum, the electron density and electron temperature is shown in Fig. 3. The electron momenta include those with phase velocities of the backward-SRS-induced Langmuir wave (p_ϕ^B) and the forward-SRS-induced Langmuir wave (p_ϕ^F). Also plotted are the maximum momenta calculated from the wave-breaking maximum electric field of the backward-SRS-induced Langmuir wave ($p_{\max}^B$) and the forward-SRS-induced Langmuir wave ($p_{\max}^F$), as well as the minimum momenta that are trapped by the backward-SRS-induced Langmuir wave ($p_{\min}^B$) and the forward-SRS-induced Langmuir wave ($p_{\min}^F$).

As shown in Fig. 3(a), the wave breaking electric field is considered in this model. If the laser intensity is strong enough and the electric field reaches the breaking limit, as in Region III, then electrons trapped by the backward-SRS-

induced Langmuir wave acquire momenta $p_{\max}^B$ larger than the minimum momentum of electrons trapped by the forward-SRS-induced Langmuir wave $p_{\min}^F$, i.e., $p_{\max}^B > p_{\min}^F$. Thus the electrons trapped by the backward-SRS-induced Langmuir wave will also be trapped and accelerated by the forward-SRS-induced Langmuir wave.

While in Region II, from the wave-breaking model, no matter how strong the laser intensity is, the electrons trapped by the backward-SRS-induced Langmuir wave acquire the maximum momenta $p_{\max}^B$ lower than the minimum momentum associated with being trapped by the forward-SRS-induced Langmuir wave $p_{\min}^F$, i.e., $p_{\max}^B < p_{\min}^F$, even after the wave breaking maximum field is reached. Thus, the two-stage electron acceleration by backward-SRS and forward-SRS cannot occur in Region II. In fact, there is another novel mechanism to accelerate the electrons: the anti-Stokes Langmuir decay instability cascade of forward-SRS. This novel mechanism accelerates the electrons to higher momenta than p_m^B, which will be clarified later.

In Region I, although there is a large gap between the electron maximum momentum trapped by the backward-SRS-induced Langmuir wave $p_{\max}^B$ and the electron minimum momentum which can be trapped by the forward-SRS-induced Langmuir wave $p_{\min}^F$, the rescattering of SRS and the Langmuir decay instability of the rescattering will accelerate the electrons trapped by the backward-SRS-induced Langmuir wave as an intermediate process.

As shown in Fig. 3(b), when the electron temperature varies, p_m^B and $p_{\min}^F$ do not vary very much. This illustrates that the electron temperature has little effect on the electron acceleration mechanisms for these conditions.

III. VLASOV SIMULATIONS

A. Laser-plasma interactions with small length-scales

In this section, we will explore the different mechanisms that accelerate electrons in the three distinct density regions first identified in Fig. 3(a) and in Table I. In addition, the new mechanism to accelerate electrons—the anti-Stokes Langmuir decay instability cascade of forward-SRS—is explored.

A one-dimensional relativistic kinetic Vlasov-Maxwell code [41–45] was used to simulate the electron cascade acceleration by the backward-SRS and the forward-SRS-induced Langmuir waves. Since the backward-SRS and the forward-SRS-induced Langmuir waves propagate in the direction of the incident laser propagation, a one-dimensional simulation is sufficient to study the effects of both processes. A hydrogen (H) plasma was taken as a typical example, as it is commonly used to model the gas fill of *Hohlraum* targets. The ion temperature was set at $T_i = T_e/3$ and the ion mass was $m_i = 1836 m_e$. The pump laser was linearly polarized and its wavelength was $\lambda_0 = 0.351$ μm. And a seed light with an intensity of $I_s = 1 \times 10^{-6} I_0$ (I_0 is the pump intensity) and a matched backward-SRS frequency was used to excite the instabilities, which was close to the thermal noise level in experiments. The spatial domain of the simulation was [0, L_x] discretized with $N_x = 5000$ spatial grid points and spatial step $dx = 0.1 c/\omega_0$, where ω_0 and c were the frequency and light speed of pump laser in vacuum. Also the spatial

length was $L_x = 500c/\omega_0$ with $2 \times 5\%L_x$ vacuum layers and $2 \times 5\%L_x$ collision layers on the two sides of the plasma boundaries. These act as strong collision damping layers to damp the electrostatic waves (such as Langmuir waves) at the boundaries, which are similar to the absorbing boundaries for the plasma. The momentum scale $[-p_{max}, p_{max}]$ was discretized with $N_p = 512$ grid points, where $p_{max} = 3m_ec$ is for electrons and $p_{max} = 0.02m_ic$ for ions (m_e is the electron static mass). The total simulation time was $t_{end} = 5 \times 10^4\omega_0^{-1}$, discretized with a time interval of $dt = 0.1\omega_0^{-1}$, to give a total time steps of $N_t = 5 \times 10^5$.

It can be seen from Fig. 3(a) that when $n_e < 0.138n_c$ (for example, $n_e = 0.1n_c, 0.12n_c$) and $T_e = 2.5$ keV, $p_{min}^F > p_{max}^B$ and the maximum momenta of the electrons are not larger than p_ϕ^F. This verifies the fact that the electrons trapped by the backward-SRS-induced Langmuir wave cannot be trapped and accelerated directly by the forward-SRS-induced Langmuir wave in Regions I and II. However, when $n_e > 0.138n_c$ (Region III), $p_{min}^F < p_{max}^B$, the electrons trapped by the backward-SRS-induced Langmuir wave are also trapped and accelerated by the forward-SRS-induced Langmuir wave. One sees that the maximum momenta from Vlasov simulations at $n_e = 0.18n_c, 0.2n_c$ are larger than the momentum (p_ϕ^F) at the phase velocity of the forward-SRS-induced Langmuir wave. This points toward the existence of a transitional density $n_e \simeq 0.138n_c$ for the electron acceleration cascade when the electron temperature is $T_e = 2.5$ keV.

One also sees that when $n_e \lesssim 0.108n_c$ (Region I), backward-SRS of forward-SRS occurs, and this accelerates electrons as an intermediate process. However, in Region II ($0.108n_c \lesssim n_e \lesssim 0.138n_c$), there are electrons with momenta larger than p_{max}^B, which cannot have been accelerated solely by the backward-SRS-induced Langmuir wave.

When the electron density is limited to $0.108n_c \lesssim n_e \lesssim 0.138n_c$, suprathermal electrons are suppressed. However, it is important to note that when the density is in the range $n_e \gtrsim 0.128n_c$, $v_L/(2\gamma_R) \equiv v_L/(2\gamma_{0R})\sqrt{v_{gs}/v_{gL}} < 1$, and $n_e \lesssim 0.128n_c$, $v_L/(2\gamma_R) > 1$, the backward-SRS process is an absolute and convective instability, respectively. This means that in order to reduce the backward-SRS reflectivity and keep the number of hot electrons to a minimum, the electron density must be limited in $n_e \lesssim 0.128n_c$ in order to maintain backward-SRS as a convective instability. Thus, the electron density in the region $0.108n_c \lesssim n_e \lesssim 0.128n_c$ (when $T_e = 2.5$ keV) is the best choice to control suprathermal electron generation and backward-SRS in indirect drive ICF.

From Fig. 3(b), $p_{min}^F < p_{max}^B$ in the parameter range $T_e \in [1, 5]$ keV. This means that the electrons trapped by backward-SRS are also trapped and accelerated by the forward-SRS provided that the laser intensity is high enough. Comparing Fig. 3(a) and 3(b), it is clear that the electron momenta are more sensitive to the electron density than the electron temperature.

To clarify the physics of the new electron acceleration mechanism in Region II, let us first discuss the two-stage electron acceleration by backward-SRS and forward-SRS in Region III, shown by Figs. 4–7 when $n_e = 0.2n_c$ and $T_e = 2.5$ keV.
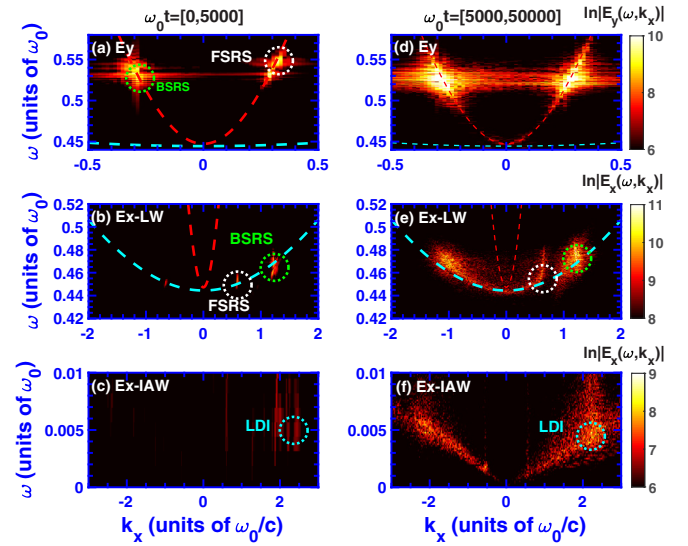

FIG. 4. The dispersion relation of [(a) and (d)] transverse electric field E_y and [(b), (c), (e), and (f)] longitudinal electric field E_x. Panels (a)–(c) are during time $t \in [0, 5000]\omega_0^{-1}$ and panels (d)–(f) are during time $t \in [5000, 50\,000]\omega_0^{-1}$. The parameters are $n_e = 0.2n_c$, $T_e = 2.5$ keV, and $I_0 = 1 \times 10^{16}$ W/cm^2 in H plasmas. The cyan dashed (bottom) line is the weakly relativistic dispersion relation of Langmuir wave [46], i.e., $\omega_L^2 = \omega_{pe}^2[1 - 5/2(v_{te}/c)^2] + 3k_L^2v_{te}^2$.
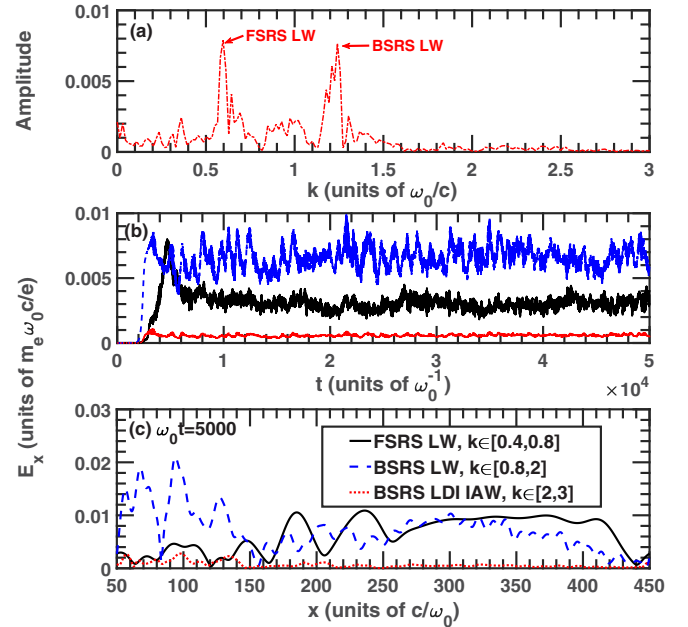

FIG. 5. (a) The wave-number spectrum of the longitudinal electric field E_x when $\omega_0t = 5000$. (b) The time evolution and (c) spatial evolution of Langmuir wave of forward-SRS ($k \in [0.4, 0.8]\omega_0/c$, solid black line), Langmuir wave of backward-SRS ($k \in [0.8, 2]\omega_0/c$, dashed blue line) and IAW of LDI of backward-SRS [$k \in [2, 3]\omega_0/c$, dotted red (bottom) line]. The electric field E_x in (b) is averaged in space $[50, 450]c/\omega_0$. The parameters are the same as Fig. 4.
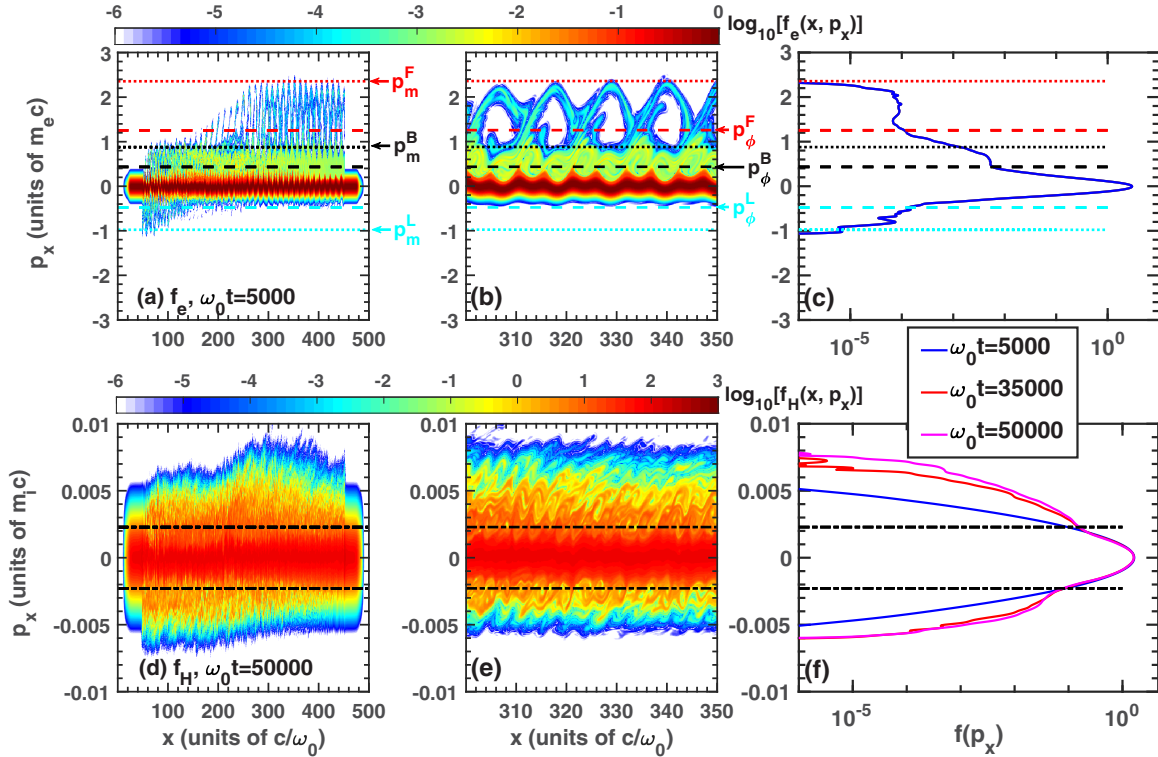
FIG. 6. The phase space of electrons in (a) the whole space region and (b) partial space region. (c) Corresponding momentum distribution averaged in space $[50, 450]c/\omega_0$ at the time of $\omega_0 t = 5000$. [(d) and (e)] The phase space of ions in the whole space region and partial space region at the time of $\omega_0 t = 5 \times 10^4$. (f) The distribution averaged in space at different times. The parameters are $n_e = 0.2n_c$, $T_e = 2.5\,\text{keV}$, and $I_0 = 1 \times 10^{16}\,\text{W}/cm^2$, the same as in Fig. 4.

1. Two-stage electron acceleration by backward-SRS and forward-SRS in Region III

Figure 4 demonstrates the spectra of the transverse electric field E_y and the longitudinal electric field E_x at different times. At early times, i.e., $\omega_0 t \in [0, 5000]$, backward-SRS and forward-SRS develop from zero to their maximum levels, and the spectra are discrete. At the same time, the Langmuir decay instability of backward-SRS develops but is not immediately obvious at this stage. In the interval $\omega_0 t \in [5000, 50000]$, backward-SRS and forward-SRS both saturate, and the spectra of backward-SRS broaden, as shown in Figs. 4(d) and 4(e), since the amplitude of the backward-SRS and the forward-SRS scattered electromagnetic waves are strong and the beam acoustic mode [47] develops. The Langmuir decay instability and its second stage, denoted as LDI2, are now more clearly observed, as shown in Figs. 4(e) and 4(f).

Figure 5 shows the wave-number spectrum [Fig. 5(a)], time evolution [Fig. 5(b)], and spatial distribution [Fig. 5(c)] of the electrostatic field E_x. From Fig. 5(a), the wave number of the backward-SRS-induced Langmuir wave is $k_L^B = 1.24\omega_0/c$ and that of the forward-SRS-induced Langmuir wave is $k_L^F = 0.597\omega_0/c$, which are close to the theoretical values $k_L^B = 1.18\omega_0/c$ and $k_L^F = 0.579\omega_0/c$.

The theoretical wave number of the ion acoustic wave generated by the Langmuir decay instability of backward-SRS is $k_{\text{IAW}} = 2.260\omega_0/c$, and this is demonstrated in Fig. 4(f) but is not so obvious in Fig. 5(a) since the ion acoustic wave from the Langmuir decay instability is much weaker than the

backward-SRS-induced Langmuir wave. Figure 5(b) shows the time evolution of the Langmuir wave of forward-SRS, the Langmuir wave of backward-SRS, and the ion acoustic wave generated by Langmuir decay instability of backward-SRS.

The backward-SRS-induced Langmuir wave increases more quickly and saturates at earlier times than the forward-SRS-induced Langmuir wave. The theoretical growth rates [29] of backward-SRS and forward-SRS are $\gamma_{tR}^B = 5.2 \times 10^{-3}\omega_0$ and $\gamma_{tR}^F = 1.9 \times 10^{-3}\omega_0$, respectively. From this, one sees that the Langmuir wave of backward-SRS increases more quickly than the Langmuir wave of forward-SRS, since $\gamma_{tR}^B > \gamma_{tR}^F$.

Figure 5(c) shows the spatial distribution of the forward-SRS-induced Langmuir wave, the backward-SRS-induced Langmuir wave, and the ion acoustic wave generated by Langmuir decay instability of backward-SRS. Backward-SRS is distributed in the entire simulation space. Among $x \in [50, 150]c/\omega_0$, backward-SRS is much stronger than the forward-SRS, thus one concludes that the electrons are only accelerated by the backward-SRS-induced Langmuir waves in this space. On the other hand, within the $x \in [150, 450]c/\omega_0$ region, forward-SRS becomes large and co-exists with backward-SRS. One therefore concludes that the two-stage acceleration of electrons occurs in this region.

Figure 6(a) shows the electron distribution in the total simulation phase space. The electrons between $x \sim [50, 150]c/\omega_0$ are only accelerated by the backward-SRS-induced Langmuir wave. Also, the electrons accelerated by the backward-SRS-induced Langmuir wave are trapped and
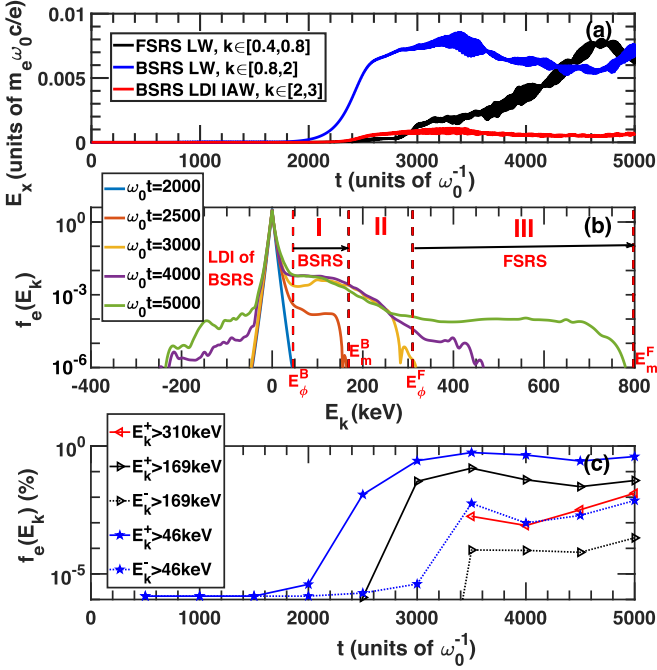
FIG. 7. (a) The time evolution of the Langmuir wave of forward-SRS ($k_L^F = 0.579\omega_0/c \in [0.4, 0.8]\omega_0/c$), the Langmuir wave of backward-SRS ($k_L^B = 1.18\omega_0/c \in [0.8, 2]\omega_0/c$), and IAW of LDI of backward-SRS ($k_A^L = 2.26\omega_0/c \in [2, 3]\omega_0/c$). The electric field E_x is averaged in space $[50, 450]c/\omega_0$. (b) The distribution of kinetic energy at different times. In our whole article, $f_e(E_k)$ represents $f_e(p_x)$ in our 1D relativistic Vlasov simulations, i.e., $f_e(E_k) \equiv f_e(p_x)$ with corresponding relation $E_k = [\sqrt{1 + (p_x/m_e c)^2} - 1]m_e c^2$, while "$f(E_k)$ (%)" with $E_k^{\pm} > \varepsilon = [\sqrt{1 + (P/m_e c)^2} - 1]m_e c^2$ means $[\int_P^{\infty} f(p_x) dp_x / \int_{-\infty}^{+\infty} f(p_x) dp_x] \times 100\%$ (+) or $[\int_{-\infty}^{-P} f(p_x) dp_x / \int_{-\infty}^{+\infty} f(p_x) dp_x] \times 100\%$ (−), respectively. (c) The evolution in time of the ratios of the electrons in different energy ranges. Label $f_e(E_k)$ (%) in vertical axis represents the ratio of the number of electrons with energy $E_k^{\pm} > E_{\text{keV}}$ to the total electron number in the system, which is in unit of %. $E_k^{\pm}$ represents the kinetic energy of electrons with positive velocity (+) and negative velocity (−). From Fig. 3, $E_\phi^B = 46 \text{ keV}$, $E_m^B = 169 \text{ keV}$, $E_\phi^F = 310 \text{ keV}$, and $E_m^F = 797 \text{ keV}$ when $n_e = 0.2n_c$, $T_e = 2.5 \text{ keV}$, and $I_0 = 1 \times 10^{16} \text{ W/cm}^2$.

gradually accelerated by the forward-SRS-induced Langmuir wave in $x \sim [150, 250]c/\omega_0$, since the electric field of the forward-SRS-induced Langmuir wave gradually increases in this region. Also, when $x \in [250, 450]c/\omega_0$, the electrons are accelerated to nearly their maximum momenta, close to the theoretical values $p_{\text{max}}^F = 2.4m_e c$.

Figure 6(b) presents a clearer demonstration of the two-stage acceleration of electrons by backward-SRS and forward-SRS in Region II ($n_e = 0.2n_c$). The electrons trapped by the backward-SRS-induced Langmuir wave are accelerated to the maximum momenta $p_{\text{max}}^B = 0.88m_e c$, which are then further trapped by the forward-SRS-induced Langmuir wave and accelerated to the maximum momenta $p_{\text{max}}^F = 2.4m_e c$. Since $p_{\text{max}}^B > p_{\text{min}}^F$, the electrons with momenta $p \in [p_{\text{min}}^F, p_{\text{max}}^B]$ are trapped by both the forward-SRS and the backward-SRS-induced Langmuir waves, this leads to the

distortion of the phase-space distribution of electrons with momenta $p \in [p_{\text{min}}^F, p_{\text{max}}^B]$.

The momentum distribution of electrons averaged in the simulation space is shown in Fig. 6(c). This shows that the distribution of electrons is flattened around the phase velocity of the backward-SRS-induced Langmuir wave, meaning that the number of electrons accelerated by the backward-SRS-induced Langmuir wave increases. When the maximum momenta of hot electrons accelerated by the backward-SRS-induced Langmuir wave are higher than the minimum momenta of electrons that are trapped by the forward-SRS-induced Langmuir wave, i.e., $p_{\text{max}}^B > p_{\text{min}}^F$, the hot electrons are further trapped and accelerated by the forward-SRS-induced Langmuir wave.

When the incident laser intensity is high enough, the Langmuir waves generated by backward-SRS and forward-SRS will be large enough to reach the maximum amplitude of electric field given by the wave breaking limit discussed in Sec. II. In our simulations with $I_0 = 1 \times 10^{16} \text{ W/cm}^2$, the maximum momentum of electrons generated by the two-stage acceleration of backward-SRS and forward-SRS is $p_m'^F = 2.3m_e c$, which is slightly lower than the theoretical value $p_{\text{max}}^F = 2.4m_e c$, since the maximum electric field in the simulation is lower than the theoretical wave breaking value.

Figures 6(d)–6(f) demonstrate the distribution of H ions. Since $n_e = 0.2n_c$, the Langmuir decay instability threshold [48] is very low, so the Langmuir decay instability of backward-SRS and the associated cascade [44] occur quite easily. Due to the combination of Langmuir decay instabilities (labelled LDI1 and LDI2 in Fig. 1), the positive directed ion acoustic wave (generated by the first Langmuir decay instability and the opposite directed ion acoustic wave by the second) will trap the H ions, as shown in Figs. 6(d)–6(f). It should be noted that the Langmuir decay instability produces a negative-propagation direction Langmuir wave which traps electrons, as shown in Fig. 6(a) and Fig. 6(c). Higher order Langmuir decay instabilities (e.g., those that might be labeled LDI3, following the nomenclature in the caption of Fig. 1) generate a Langmuir wave with higher phase velocity, thus the maximum momentum of negative directed electrons is larger than the theoretical value p_{max}^L which considers only the first stage of the Langmuir decay instability.

As shown in Fig. 7(a), the backward-SRS-induced Langmuir wave develops from $t \simeq 2000\omega_0^{-1}$ and saturates at $t \simeq 3400\omega_0^{-1}$, while the forward-SRS-induced Langmuir wave develops from $t \simeq 2500\omega_0^{-1}$ and saturates at $t \simeq 4800\omega_0^{-1}$.

Figure 7(b) shows that, at $\omega_0 t = 2000$, the distribution of electrons is initially Maxwellian and the electrons are not accelerated. There are three processes associated with the two-stage electron acceleration by backward-SRS and forward-SRS.

Process I: The backward-SRS-induced Langmuir wave only accelerates the electrons from $E_\phi^B = 46 \text{ keV}$ to $E_m^B = 169 \text{ keV}$ during $\omega_0 t \simeq [2000, 2500]$.

Process II: The low-amplitude forward-SRS-induced Langmuir wave traps the electrons that are accelerated by the backward-SRS-induced Langmuir wave during $\omega_0 t \simeq [2500, 3000]$, the energy gap is from $E_m^B = 169 \text{ keV}$ to $E_\phi^F = 310 \text{ keV}$.
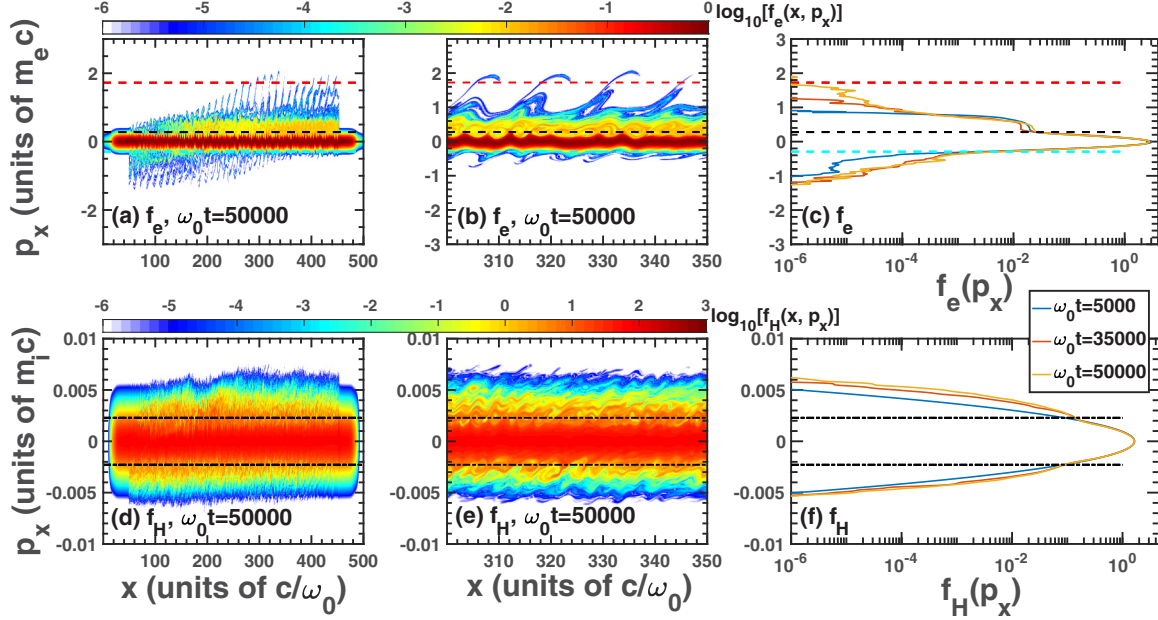
FIG. 8. The phase space of electrons in (a) the total space region and (b) partial space region, and (c) corresponding distribution averaged in space range $[50, 450]c/\omega_0$. [(d) and (e)] The phase space of ions in the total space region and partial space region at the time of $\omega_0 t = 5 \times 10^4$. (f) The distribution averaged in space at different time. The parameters are $n_e = 0.15 n_c$, $T_e = 2.5$ keV, and $I_0 = 1 \times 10^{16}$ W/cm^2.

Process III: The large-amplitude forward-SRS-induced Langmuir wave traps and accelerates electrons from $E_\phi^F = 310$ keV to nearly $E_m^F = 797$ keV during $\omega_0 t \simeq [3000, 5000]$.

The electron ratio is shown in Fig. 7(c). The ratio of electrons with energy larger than $E_\phi^B = 46$ keV develops from 3.9×10^{-6}% to 0.56% when the time varies from $\omega_0 t = 2000$ to $\omega_0 t = 3500$. When $\omega_0 t > 3500$, the ratio of electrons with $E_k > 46$ keV trapped by the backward-SRS-induced Langmuir wave decreases due to the saturation and decrease of the backward-SRS-induced Langmuir wave amplitude as shown in Fig. 7(a). The ratio of hot electrons with $E_k > E_m^B = 169$ keV develops from 1.2×10^{-6}% to 0.14% when the time varies from $\omega_0 t = 2500$ to $\omega_0 t = 3500$ and then saturates and decreases after $\omega_0 t = 3500$, which is consistent to the backward-SRS-induced Langmuir wave amplitude. This part of electrons with $E_k^+ \in [E_m^B, E_\phi^F]$ are trapped by the backward-SRS-induced Langmuir wave to reach E_m^B and then trapped by the forward-SRS-induced Langmuir wave. As a result, they are related to the backward-SRS-induced Langmuir wave amplitude.

The ratio of electrons with $E_k^+ > E_\phi^F = 310$ keV is from 1.8×10^{-3}% to 0.014% when the time varies from $\omega_0 t = 3500$ to $\omega_0 t = 5000$. These electrons are only accelerated by the large-amplitude forward-SRS-induced Langmuir wave. The number of negative-direction propagating electrons with $E_k^- > 46$ keV and $E_k^- > 169$ keV is very small as shown in Fig. 7(c), which are generated by the Langmuir decay instability of backward-SRS. Although the number of suprathermal electrons with $E_k^+ > E_m^F = 310$ keV is very small, the kinetic energy of these electrons are very high, which preheat the fusion fuel.

2. Electron acceleration by anti-Stokes Langmuir decay instability cascade in Region II

When the electron density decreases from $n_e = 0.2 n_c$ (Fig. 6) to $n_e = 0.15 n_c$ (Fig. 8) to $n_e = 0.13 n_c$ (Fig. 9) to $n_e = 0.12 n_c$ (Fig. 10) in descending order, the maximum momentum, and therefore the kinetic energy of the trapped electrons, decreases. As shown in Figs. 8(a) and 8(b), the electrons trapped and accelerated by the backward-SRS-induced Langmuir wave are further trapped by the forward-SRS-induced Langmuir wave, although the forward-SRS-induced vortices shaping the electron phase spaces when $n_e = 0.15 n_c$ are less obvious than those when $n_e = 0.2 n_c$.

The threshold electron density ($n_e = 0.138 n_c$) beyond which electrons can be accelerated via the backward-SRS and the forward-SRS process is estimated assuming the backward-SRS-induced Langmuir wave reaches the wave breaking limit, as analytically evaluated in Refs. [36,38]. Those waves, however, can saturate at a lower amplitude due to Langmuir decay instability [9,44], sideband-type instabilities [49,50], so that the model only gives an approximate lower limit of the threshold density for backward-SRS and forward-SRS coupling. There are indeed a few electrons with momentum larger than the phase velocity of the forward-SRS-induced Langmuir wave, which verifies that the two-stage acceleration of backward-SRS and forward-SRS occurs when the electron density is $n_e = 0.15 n_c$ in Region III as shown in Fig. 8(b).

While in the Region II as shown in Fig. 3(a), two cases for $n_e = 0.13 n_c$ and $n_e = 0.12 n_c$ are chosen as examples. As shown in Figs. 9(a)–9(c) and Figs. 10(a)–10(c), none of electrons are trapped and accelerated by the forward-SRS-induced Langmuir wave. The maximum momenta of electrons at any time do not exceed that at the phase velocity of
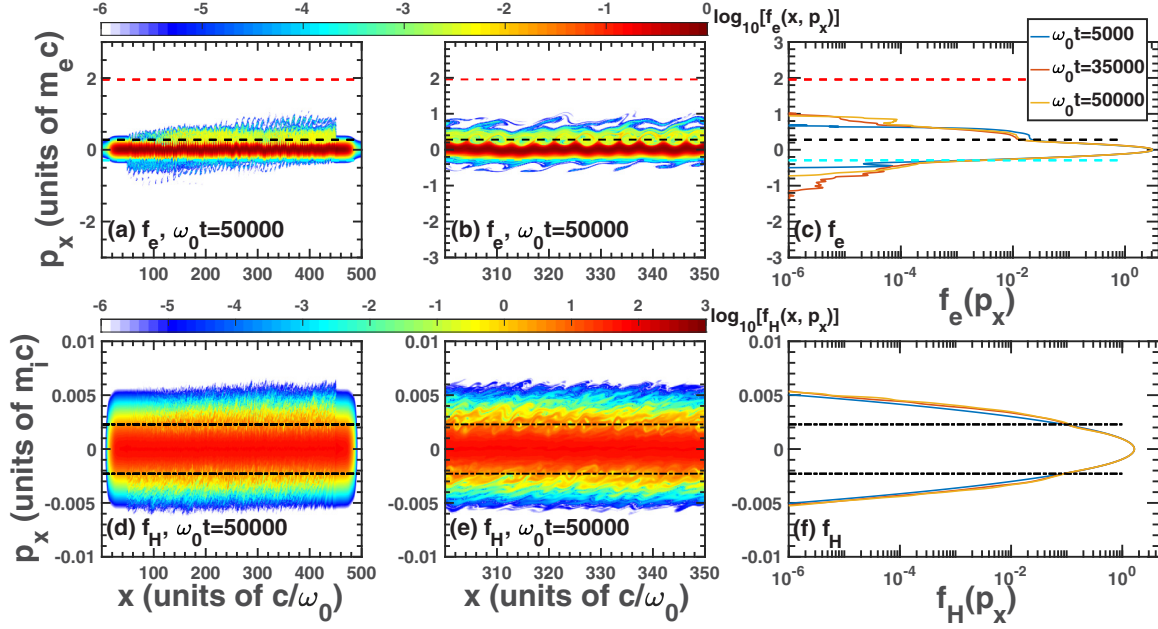
FIG. 9. The phase space of electrons in (a) the whole space region and (b) partial space region. (c) Corresponding distribution averaged in space $[50, 450]c/\omega_0$. [(d) and (e)] The phase space of ions in the total space region and partial space region at the time of $\omega_0 t = 5 \times 10^4$. (f) The distribution averaged in space at different times. The parameters are $n_e = 0.13 n_c$, $T_e = 2.5$ keV, and $I_0 = 1 \times 10^{16}$ W/cm^2.

the forward-SRS-induced Langmuir wave. The electron momentum remains at a low level. However, there is a small number of electrons with momenta larger than p_{max}^B (the maximum electron momentum accelerated by the backward-SRS-induced Langmuir wave). These energetic electrons with momenta larger than p_{max}^B are due to the generation of Langmuir waves with higher phase velocity than the backward-SRS-induced Langmuir wave, which is from the

second-stage anti-Stokes Langmuir decay instability (ALDI2) of forward-SRS, which will be clarified in the next paragraph.

The negative propagation electrons are generated by the Langmuir wave of the first or third anti-Stokes Langmuir decay instability (ALDI1 or ALDI3) of forward-SRS, but not from the Langmuir decay instability of backward-SRS. When $n_e = 0.12$ or $0.13 n_c$, the Langmuir decay instability of backward-SRS is difficult excite, because this is in the kinetic
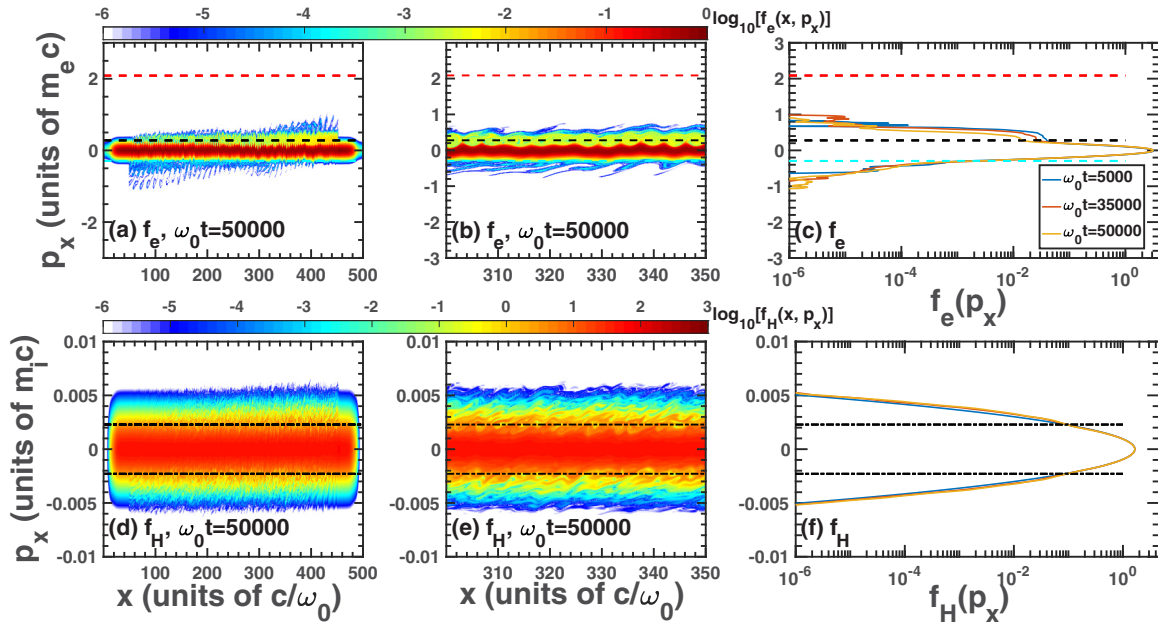

FIG. 10. The phase space of electrons in (a) the whole space region and (b) partial space region. (c) Corresponding distribution averaged in space range $[50, 450]c/\omega_0$. [(d) and (e)] The phase space of ions in the total space region and partial space region at the time of $\omega_0 t = 5 \times 10^4$. (f) The distribution averaged in space at different times. The parameters are $n_e = 0.12 n_c$, $T_e = 2.5$ keV, and $I_0 = 1 \times 10^{16}$ W/cm^2.
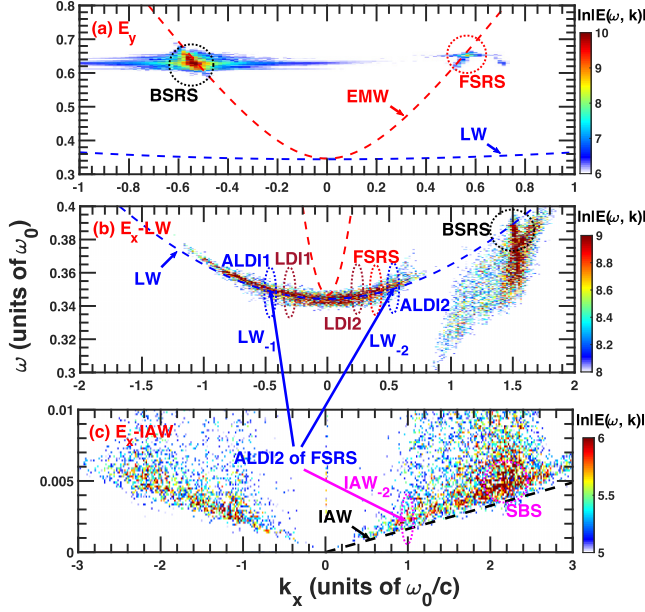
FIG. 11. The dispersion relation of (a) transverse electric field E_y and [(b) and (c)] longitudinal electric field E_x. Where (a)–(c) are during the time range $t \in [5000, 50\,000]\omega_0^{-1}$ and the space range $x \in [100, 400]c/\omega_0$. The parameters are $n_e = 0.12n_c$, $T_e = 2.5$ keV, and $I_0 = 1 \times 10^{16}$ W/cm^2 in H plasmas.

regime [27,28]. The green (light gray) lines in Figs. 9(c) and 10(c) represent the momenta at the phase velocity of the Langmuir wave from the Langmuir decay instability of backward-SRS, one sees that nearly no negative propagation electrons are trapped around those momenta.

To confirm that there exists a Langmuir wave that has a higher phase velocity than the backward-SRS-induced Langmuir wave, the dispersion relation is plotted in Fig. 11. When $n_e = 0.12n_c$, the wave number of the backward-SRS-induced Langmuir wave is $k_L^B \lambda_{De} = 0.29$, which is in the kinetic regime [51]. Thus, the Langmuir decay instability of backward-SRS is not allowed. However, the wave number of the forward-SRS-induced Langmuir wave is $k_L^F = 0.39\omega_0/c = 0.078\lambda_{De}^{-1}$, which means it is in the fluid regime [27,28]. Thus, the Langmuir decay instability cascade of the forward-SRS occurs more easily and the anti-Stokes process of the Langmuir decay instability is generated in the cascade. As shown in Fig. 11(b), there is no Langmuir decay instability of backward-SRS-induced Langmuir wave, and the cascade of the forward-SRS-induced Langmuir wave is very large, consistent with the theory. The wave number of Langmuir waves generated by the n-stage Langmuir decay instability (denoted as LDIn) of forward-SRS-induced Langmuir wave (k_L^F) is given by

$$k_{Ln} \simeq (-1)^n \left(\left| k_L^F \right| - n \cdot \Delta k \right), \quad (6)$$

where $\Delta k = \frac{2}{3}\frac{1}{\lambda_{De}}\frac{c_s}{v_{te}}$, and the negative sign represents the propagation direction of the Langmuir wave. When $n_e = 0.12n_c$ and $T_e = 2.5$ keV, one obtains $\Delta k = 0.0156\lambda_{De}^{-1} = 0.0771\omega_0/c$. Thus, $k_{L1} = -0.31\omega_0/c$ from LDI1 of forward-SRS, $k_{L2} = 0.23\omega_0/c$ from LDI2 of forward-SRS. The n-stage anti-Stokes LDI (ALDIn) of forward-SRS-induced
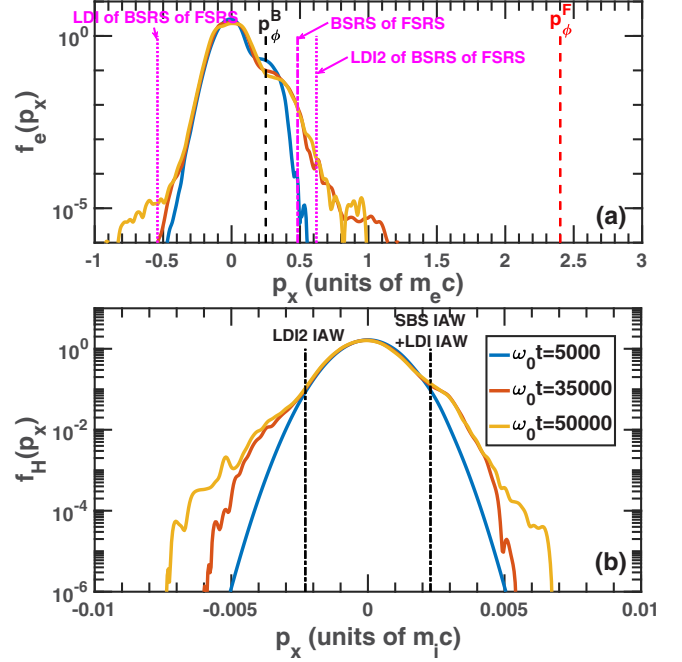

FIG. 12. The distributions of (a) electrons and (b) H ions averaged in total simulation space at different time. Where the simulation condition is $n_e = 0.1n_c$, $T_e = 2.5$ keV, and $I_0 = 5 \times 10^{16}$ W/cm^2 in H plasmas.

Langmuir wave is given by

$$k_{L-n} \simeq (-1)^n \left(\left| k_L^F \right| + n \cdot \Delta k \right), \quad (7)$$

thus $k_{L-1} = -0.46\omega_0/c$ and $k_{L-2} = 0.54\omega_0/c$ from the anti-Stokes Langmuir decay instability 1 and 2 (ALDI1 and ALDI2) of forward-SRS, respectively. When the wave number of ALDI2 is $k_{L-2} = 0.54\omega_0/c$, the corresponding phase velocity, electron momenta, and kinetic energy of the electrons are $v_{\phi-2} = 0.65c$, $p_{\phi-2} = 0.86m_ec$, and $E_{\phi-2} = 161$ keV at this particular phase velocity. The portion of energetic electrons with momenta larger than $p_{max}^B = 0.60m_ec$ ($E_m^B = 84$ keV) shown in Fig. 10(c). The clearer results of this novel mechanism will be further demonstrated in Secs. III B and IV. This is due to generation of the Langmuir wave (labelled as LW$_{-2}$) from the second-stage anti-Stokes Langmuir decay instability (ALDI2) of forward-SRS.

3. Electron acceleration by rescattering and Langmuir decay instability cascade in Region I

As shown in Fig. 3(a), $p_{min}^F > p_{max}^B$ when $n_e = 0.1n_c$, $T_e = 2.5$ keV (Region I). Therefore, the electrons trapped by the backward-SRS-induced Langmuir wave cannot be trapped and accelerated by the forward-SRS-induced Langmuir wave directly. To verify this conclusion, we have conducted Vlasov simulations for $n_e = 0.1n_c$, $T_e = 2.5$ keV, and $I_0 = 5 \times 10^{16}$ W/cm^2 as shown in Fig. 12. The backward-SRS gain $G_R = 3.4$ when $I_0 = 1 \times 10^{16}$ W/cm^2 is very small, and as such both backward-SRS and forward-SRS experience low growth in Vlasov simulations when there is no seed electromagnetic wave. Thus a large intensity $I_0 = 5 \times 10^{16}$ W/cm^2 is used in this case. The electrons trapped

by the backward-SRS-induced Langmuir wave cannot be trapped by the forward-SRS-induced Langmuir wave indeed even when $\omega_0 t = 50\,000$. When $n_e = 0.1 n_c$, backward-SRS of backward-SRS cannot occur because it is not possible to satisfy the three-wave matching conditions, and the Langmuir decay instability of backward-SRS is difficult to be excited. Backward-SRS of forward-SRS, Langmuir decay instability of backward-SRS of forward-SRS, and a second-stage Langmuir decay instability (LDI2) of backward-SRS of forward-SRS are presented, as shown in Fig. 12(a). These rescattering and Langmuir decay instability processes further accelerate electrons that are trapped by the backward-SRS-induced Langmuir wave. However, in this section, the plasma length is not very large, thus forward-SRS, backward-SRS of forward-SRS, and the Langmuir decay instability cannot develop to a significant level. As a result, the forward-SRS-induced Langmuir wave is not able to trap low-momenta electrons. On the other hand, if the plasma density length is large enough, then the rescattering will accelerate the electrons to sufficiently high energy to be trapped by the forward-SRS-induced Langmuir wave [17]. SBS can also exist in this parameter regime. The corresponding ion acoustic waves generated by stimulated Brillouin scattering, the Langmuir decay instability or the second-stage Langmuir decay instability (LDI2) flatten the ion distribution at their phase velocity, as shown in Fig. 12(b).

B. Laser-plasma interactions with large length scales

In this section, we will explore the effect of the spatial scale on these different processes using the Vlasov simulation tool described previously. The spatial scale was set at $[0, L_x]$ and discretized with $N_x = 50\,000$ spatial grid points and spatial step $dx = 0.1 c/\omega_0$. The spatial length was $L_x = 5000 c/\omega_0$ with $2 \times 5\% L_x$ vacuum layers with $2 \times 5\% L_x$ collision layers on either sides of the plasma column. The pump intensity was $I_0 = 3 \times 10^{15}$ W/cm^2. The other parameters were the same as those described in Sec. III A.

As shown in Fig. 13, when $n_e = 0.2 n_c$, $L_x = 5000 c/\omega_0$ (Region III), the two-stage acceleration by backward-SRS and forward-SRS occurs. This is similar to the results obtained for when the parameters were $n_e = 0.2 n_c$, $L_x = 500 c/\omega_0$, although the pump light intensity is $I_0 = 3 \times 10^{15}$ W/cm^2, somewhat lower than that in the short plasma simulations shown in Sec. III A. Figure 14(a) shows that when $\omega_0 t = 1 \times 10^4$, only the backward-SRS-induced Langmuir wave traps and accelerates electrons. After $\omega_0 t \simeq 2 \times 10^4$, the forward-SRS-induced Langmuir wave traps and accelerates electrons to a maximum energy of approximately 700 keV, which is slightly lower than the maximum limit energy $E^F_{\max} = 797$ keV from analytic theory. At the same time, the Langmuir wave generated from the Langmuir decay instability of backward-SRS traps electrons and produces negative propagation energetic electrons after $\omega_0 t \simeq 2 \times 10^4$.

The ratios of electrons with energy above the energy corresponding to phase velocities of different Langmuir waves from backward-SRS (46 keV), Langmuir decay instability of backward-SRS (55 keV), and forward-SRS (309 keV) are shown in Fig. 14(b). The saturation level of energetic electrons with $E_k > 46$ keV accelerated by the backward-SRS-induced
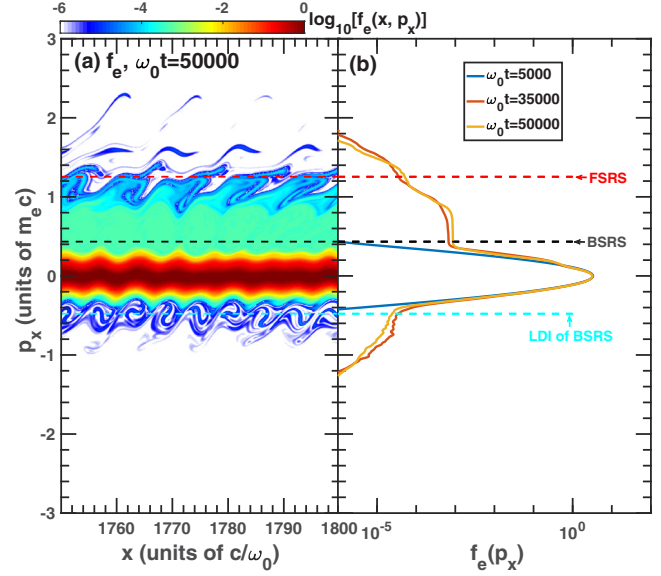

FIG. 13. (a) The phase space of electrons and (b) the corresponding electron distribution function averaged in space across $[1750, 1800] c/\omega_0$. The parameters are $n_e = 0.2 n_c$, $T_e = 2.5$ keV, and $I_0 = 3 \times 10^{15}$ W/cm^2 in H plasmas with $L_x = 5000 c/\omega_0$.

Langmuir wave is $\sim 0.1\%$, while the level of energetic electrons with $E_k > 309$ keV accelerated by the forward-SRS-induced Langmuir wave is $\sim 0.01\%$. These results illustrate that the two-stage acceleration of electrons by backward-SRS and forward-SRS occurs when $n_e = 0.2 n_c$ in both long ($L_x = 5000 c/\omega_0$) and short ($L_x = 500 c/\omega_0$) scale plasma.

Let us examine what happens when the electron density $n_e = 0.12 n_c$, i.e., in Region II [shown in Fig. 3(a)]. Figure 15 shows that the electrons are trapped and accelerated by the backward-SRS-induced Langmuir wave but cannot be trapped by the forward-SRS-induced Langmuir wave due to a large gap between the phase velocities of the forward-SRS and backward-SRS-induced Langmuir waves.

The maximum momentum of electrons trapped by the backward-SRS-induced Langmuir wave reaches only $p^B_{\max} = 0.60 m_e c$ from the wave-breaking limit. However, there is a tail of energetic electrons with momenta larger than $p^B_{\max}$. These electrons are trapped and accelerated by a Langmuir wave with a higher phase velocity arising from the second-stage anti-Stokes Langmuir decay instability ALDI2 of forward-SRS, as demonstrated above in Fig. 11.

The momentum at phase velocity of the Langmuir wave is $p_{\phi-2} = 0.86 m_e c$, which is indeed at the energetic electron tail. Although electrons are accelerated by backward-SRS and ALDI2 of forward-SRS to momenta of nearly $p_{\max} \sim 1.4 m_e c$, this is also much lower than the momenta at the phase velocity of the forward-SRS $p^F_\phi = 2.1 m_e c$. Since there exists a number of saturation mechanisms of both backward-SRS and forward-SRS, such as sideband instability of backward-SRS [49,50] and Langmuir decay instability of forward-SRS [9,44], there is a maximum electric field that cannot approach the wave-breaking limit. Therefore, the electrons accelerated by ALDI2 of forward-SRS cannot be trapped and accelerated by forward-SRS as shown in Fig. 15.
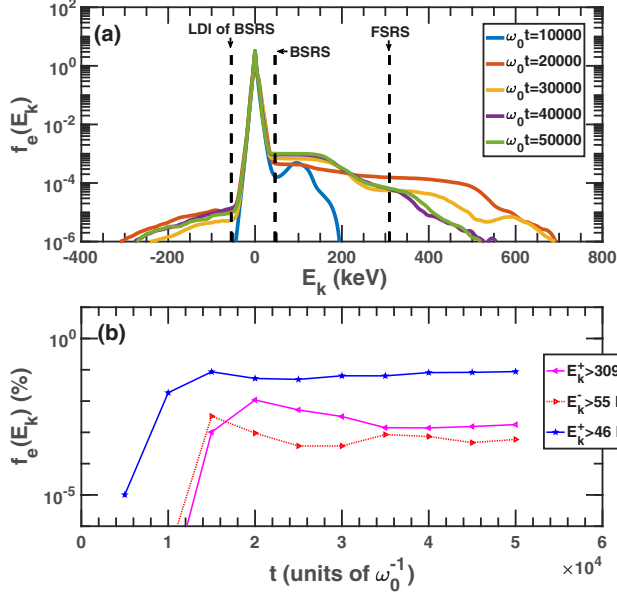
FIG. 14. (a) The distribution of electron kinetic energy at different times, spatially averaged over the range $[1000, 4000]c/\omega_0$. (b) The evolution in time of the ratios of the electrons in different energy ranges. The black dashed lines labeled in (a) represent the phase velocities of corresponding Langmuir waves. $E_k^{\pm}$ represents the kinetic energy of the electrons with positive velocity $(+)$ and negative velocity $(-)$. From theoretical considerations, $E_{\phi}^B = 46$ keV, $E_{\phi}^F = 309$ keV, and $E_{\phi}^L = 55$ keV from LDI of backward-SRS when $n_e = 0.2n_c$, $T_e = 2.5$ keV, $I_0 = 3 \times 10^{15}$ W/cm^2, and $L_x = 5000c/\omega_0$.

From the energy spectrum shown in Fig. 16(a), the electrons are solely trapped and accelerated by the backward-SRS-induced Langmuir wave before $\omega_0 t \sim 1 \times 10^4$. When $\omega_0 t = 2 \times 10^4$, more energetic electrons are generated around $E_{\phi-2} = 161$ keV. This is the Langmuir wave from ALDI2 of forward-SRS. The maximum energy reaches nearly 400 keV, but the electrons cannot yet be trapped and accelerated by the forward-SRS-induced Langmuir wave ($E_{\phi}^F = 672$ keV).

The evolution of electron ratios with different energy windows is shown in Fig. 16(b). After $\omega_0 t \sim 1 \times 10^4$, the electrons with energy above $E_{\phi}^B = 20$ keV nearly saturate, which illustrates that backward-SRS saturates after $\omega_0 t \sim 1 \times 10^4$. Also, the electrons with energy above $E_m^B = 84$ keV are generated from the Langmuir wave of ALDI2 of forward-SRS, the ratio of which is about 0.01%. Finally, the electrons with energy above $E_{\phi}^F = 672$ keV result in a ratio nearly equal to zero and can therefore be neglected.

Let us now turn our attention to the situation when the electron density is $n_e = 0.1n_c$ in order to illustrate what happens in Region I [shown in Fig. 3(a)]. It is clear that the laser pulse interaction with large scale plasma produces rescatterings and corresponding Langmuir decay instabilities, as shown in Fig. 17.

Here the phase velocity of the forward-SRS-induced Langmuir wave is now much higher than that of the backward-SRS-induced Langmuir wave. This means that the electrons accelerated by the backward-SRS-induced Langmuir wave cannot be trapped and accelerated by the forward-SRS-induced Langmuir wave directly. Rather, under these partic-
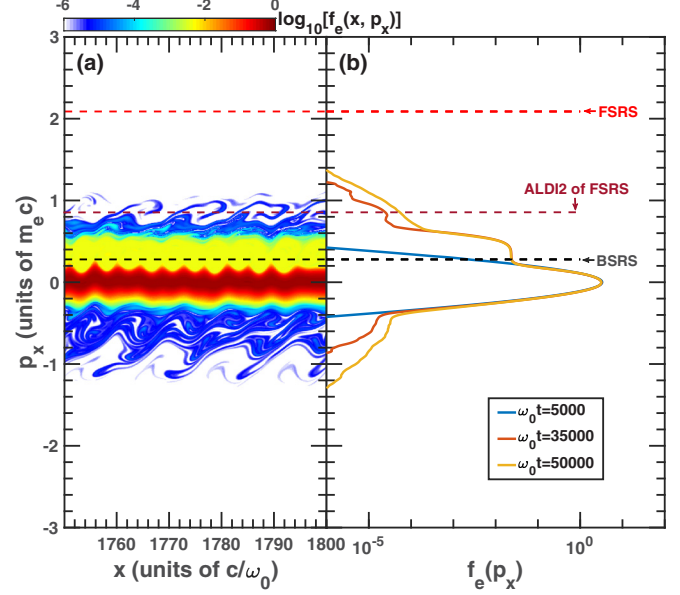
FIG. 15. (a) The phase space of electrons and (b) the corresponding electron distribution function averaged in space across $[1750, 1800]c/\omega_0$. The parameters are $n_e = 0.12n_c$, $T_e = 2.5$ keV, and $I_0 = 3 \times 10^{15}$ W/cm^2 in H plasmas with $L_x = 5000c/\omega_0$.

ular conditions, only backward-SRS of forward-SRS occurs. Since the wave number of the backward-SRS-induced Langmuir wave is $k_L^B \lambda_{\mathrm{De}} = 0.33$, this means that the process is in the kinetic regime. Thus the Langmuir decay instability of backward-SRS is marginal for growth.

On the other hand, the wave number of backward-SRS of forward-SRS-induced Langmuir wave is $k_L^r \lambda_{\mathrm{De}} = 0.17$. This is in the fluid regime. Thus the Langmuir decay instability cascade associated with this rescattering does occur more easily. At the same time, the Langmuir decay instability cascade of forward-SRS-induced Langmuir wave ($k_L^F \lambda_{\mathrm{De}} = 0.076$) also grows more easily.

The backward-SRS of forward-SRS and Langmuir decay instability cascade of backward-SRS of forward-SRS produce Langmuir waves with higher phase velocities than the backward-SRS-induced Langmuir waves. Therefore, the cascade process provides the mechanism for electrons to be accelerated from low to high energy.

The maximum momenta that electrons can acquire is nearly $p_x \sim 2.2 m_e c$, as illustrated in Fig. 17(b), and the maximum energy is $E_k \sim 820$ keV, as shown in Fig. 18(a). This is close to $E_{\phi}^F = 818$ keV. This provides conclusive evidence that when the electron density is $n_e \lesssim 0.108n_c$ (Region I), the cascade acceleration mechanism by backward-SRS, rescatterings, Langmuir decay instability of rescatterings and forward-SRS occur [17]. These instabilities also accelerate electrons to high energy.

IV. ONE- AND THREE-DIMENSIONAL PARTICLE-IN-CELL SIMULATIONS

The 1D and 3D Particle-in-Cell (PIC) code EPOCH [52,53] was used to investigate the hot electron generation mechanisms from the different instabilities to confirm the
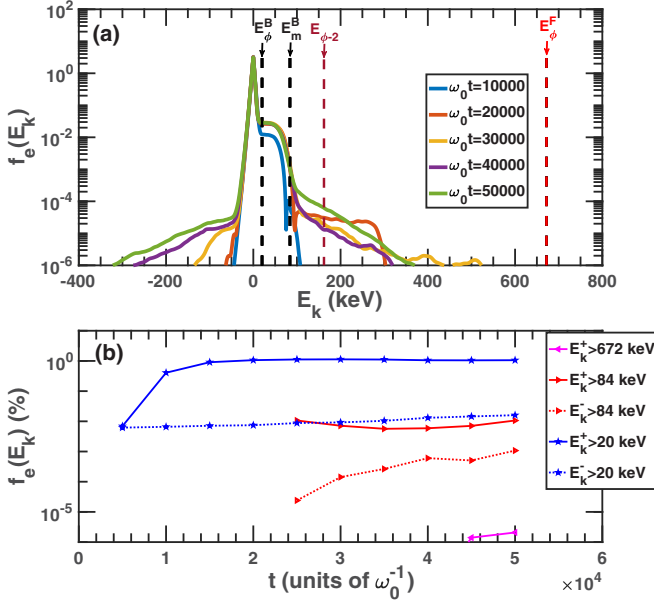
FIG. 16. (a) The distribution of electron kinetic energy at different times. (b) The evolution in time of the ratios of the electrons in different energy ranges. The black dashed lines labeled in (a) represent the phase velocities of corresponding Langmuir waves. $E_k^{\pm}$ represents the kinetic energy of electrons with positive velocity (+) and negative velocity (−). From theoretical calculation, $E_\phi^B = 20$ keV, $E_m^B = 84$ keV, $E_{\phi-2} = 161$ keV, and $E_\phi^F = 672$ keV when $n_e = 0.12n_c$, $T_e = 2.5$ keV, $I_0 = 3 \times 10^{15}$ W/cm^2, and $L_x = 5000c/\omega_0$.

veracity of the results in Sec. II when extrapolated to higher dimensions (this was not possible with the Vlasov code due to the available computational resources).

The electron/ion and laser pulse conditions were the same as that in Sec. III B, i.e., the electron temperature was $T_e = 2.5$ keV and electron density is $n_e = 0.1, 0.12, 0.2n_c$, where n_c was the critical density of the incident pump light. The ion temperature was $T_i = T_e/3$, the same as that in Vlasov simulations. The pump laser pulse intensity was $I_0 = 3 \times 10^{15}$ W/cm^2 with a plane wave envelope and linear polarization in the y direction for both 1D and 3D simulations.

In the 1D simulations, the spatial domain along the x direction was set at $[0, 800\lambda_0]$ discretized with $N_x = 2 \times 10^4$ spatial grid points and spatial step $dx = 0.04\lambda_0$. The particles occupied the full simulation space of the box with no vacuum layer on either side of the plasma slab. The total simulation time was $t_{end} = 8000T_0 = 9.4$ ps, where $T_0 = 1.17$ fs was the period of 3ω pump light (351 nm).

In 3D simulations, the simulation parameters were the same as those in the 1D simulations, but the spatial domains in y and z directions were $[-5\lambda_0, 5\lambda_0]$ and $[-5\lambda_0, 5\lambda_0]$ discretized with $N_y = 10$ and $N_z = 10$ spatial grid points. Open boundary conditions for the laser and thermal particles were used in the x direction for both 1D and 3D simulations, and periodic boundaries were used in y and z directions for the 3D simulations. There were 1000 electrons and 1000 ions per cell in the 1D simulations and 10 electrons/ions per cell in the 3D simulations.
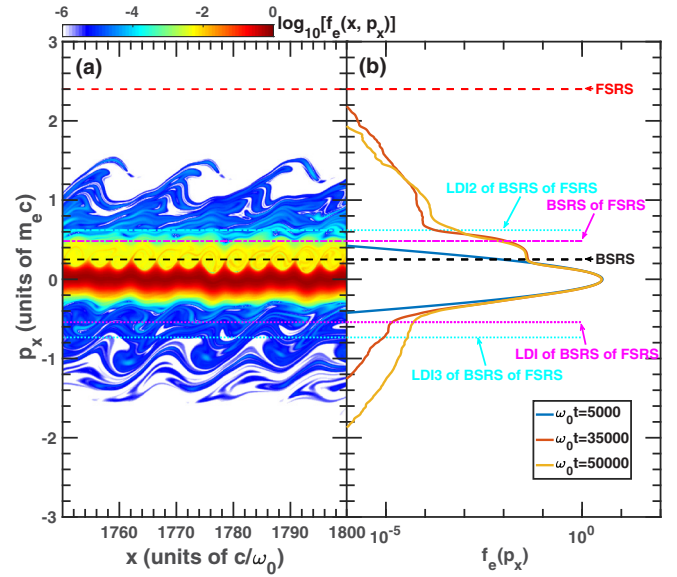

FIG. 17. (a) The phase space of electrons and (b) the corresponding electron distribution function averaged in space across $[1750, 1800]c/\omega_0$. The parameters are $n_e = 0.1n_c$, $T_e = 2.5$ keV, and $I_0 = 3 \times 10^{15}$ W/cm^2 in H plasmas with $L_x = 5000c/\omega_0$.
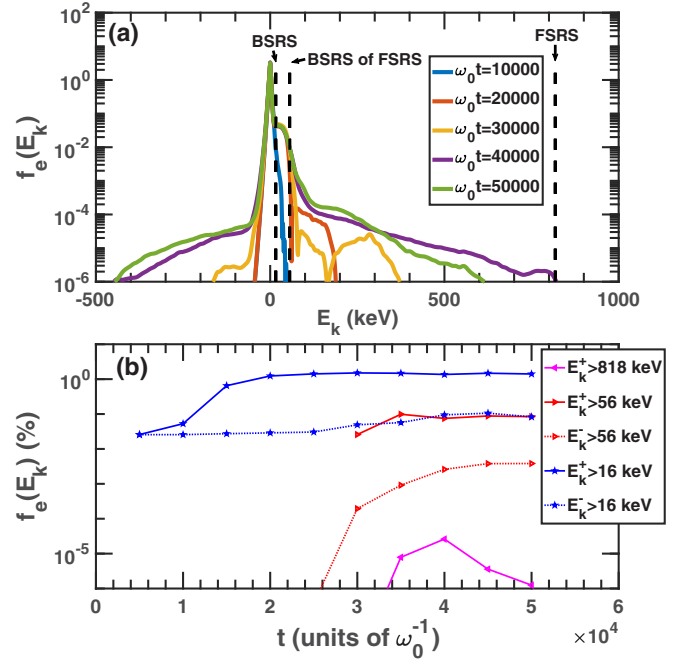

FIG. 18. (a) The distribution of electron kinetic energy at different times. (b) The evolution in time of the ratios of the electrons in different energy ranges. The black dashed lines labeled in (a) represent the kinetic energy at the phase velocities of corresponding Langmuir waves. $E_k^{\pm}$ represents the kinetic energy of electrons with positive velocity (+) and negative velocity (−). From theoretical calculation, $E_\phi^B = 16$ keV, $E_\phi^F = 818$ keV, and $E_\phi^r = 56$ keV from the rescattering backward-SRS of forward-SRS when $n_e = 0.1n_c$, $T_e = 2.5$ keV, $I_0 = 3 \times 10^{15}$ W/cm^2, and $L_x = 5000c/\omega_0$.
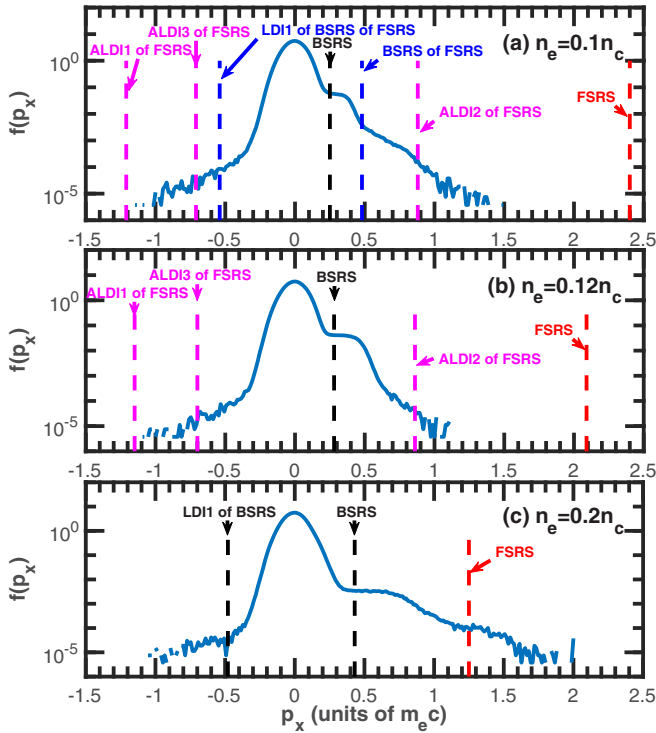
FIG. 19. The electron distribution functions from 1D EPOCH simulations when (a) $n_e = 0.1n_c$, (b) $n_e = 0.12n_c$, and (c) $n_e = 0.2n_c$ at the time of $t = 2000T_0$, which are spatially averaged across the whole length of the simulation domain along the x direction $[0, 800\lambda_0]$. The other parameters are $T_e = 2.5\,\text{keV}$, $I_0 = 3 \times 10^{15}$ W/cm^2 in H plasmas with $L_x = 800\lambda_0$.

FIG. 20. The electron distribution of (a) p_x, (d) p_y, and (f) p_z from 3D EPOCH simulations, which are averaged across the whole length of the simulation's domain along the x direction $[0, 800\lambda_0]$. (b) The phase space $(x - px)$ of electrons. The electron momentum distribution across (c) x and y, (e) x and z. The time is $t = 5600T_0$ and the parameters are $n_e = 0.12n_c$, $T_e = 2.5\,\text{keV}$, and $I_0 = 3 \times 10^{15}$ W/cm^2 for the H plasmas considered in the simulations.

Figure 19 shows the 1D simulations results for $n_e = 0.1, 0.12$, and $0.2n_c$. The parameters were the same as those described in Sec. III B. When $n_e = 0.1n_c$ (Region I) shown in Fig. 19(a), the electrons are first trapped by the backward-SRS-induced Langmuir wave, then mainly accelerated by the Langmuir waves from backward-SRS of forward-SRS and the corresponding Langmuir decay instability cascade of this rescattering. At the same time, the Langmuir waves induced by anti-Stokes Langmuir decay instability cascade of forward-SRS are also shown in Fig. 19(a), which promote the acceleration of electrons.

When $n_e = 0.12n_c$ (Region II), shown in Fig. 19(b), the electrons are trapped and accelerated by the backward-SRS, anti-Stokes Langmuir decay instability cascade of forward-SRS-induced Langmuir waves. The phase velocities of Langmuir waves induced by these instabilities labeled in Fig. 19 are shown in Table I.

When $n_e = 0.2n_c$ (Region III), shown in Fig. 19(c), the electrons are trapped and accelerated by backward-SRS and forward-SRS directly, and the negative propagating electrons are accelerated by the Langmuir decay instability of backward-SRS. This is because no rescatterings exist for these conditions. Also, both backward-SRS and forward-SRS are much stronger than corresponding Langmuir decay instability. Consequently, the principal acceleration mechanisms are dual-stage electron acceleration by backward-SRS and forward-SRS. The results from the 1D PIC simulations are
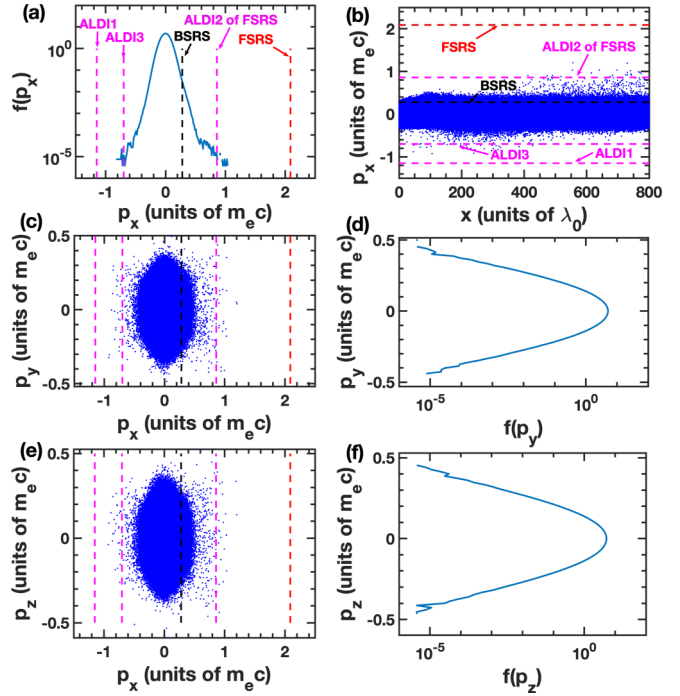
close to those obtained by 1D Vlasov simulations, as shown in Sec. III B, which illustrate that the results are robust between the simulation methods.

To further understand the electron acceleration processes in 3D, multidimensional PIC simulations were also performed. Figure 20 shows the electron distributions of momenta p_x, p_y, and p_z when $n_e = 0.12n_c$ (Region II). Figure 20(a) demonstrates that the electrons are trapped by the backward-SRS-induced Langmuir wave and there are higher momenta tails in the electron distribution. The positive momenta correspond to the phase velocity of the Langmuir wave from the second-stage anti-Stokes Langmuir decay instability ALDI2 of forward-SRS, while the negative momenta are associated with the third-stage anti-Stokes Langmuir decay instability ALDI3 of forward-SRS. This illustrates that the anti-Stokes Langmuir decay instability cascade of forward-SRS is the precise mechanism to accelerate electrons to higher momenta when $n_e = 0.12n_c$.

The snapshots of the electron distribution [Fig. 20(a)] and the electron phase space $(x - px)$ [Fig. 20(b)] are nearly identical to those generated by both the 1D EPOCH simulations [Fig. 19(b)] and the 1D Vlasov simulations (Fig. 15). This confirms that the mechanism of electron acceleration by anti-Stokes Langmuir decay instability cascade of forward-SRS is robust.

Figures 20(c)–20(f) show the momenta distributions of electrons in both the y and z directions. The electrons have a near-Maxwellian distribution and are not accelerated in the
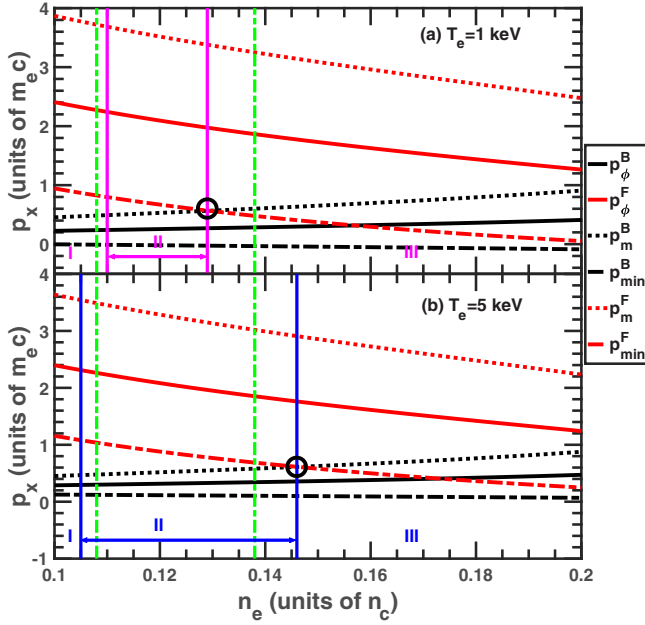
FIG. 21. The variation of p_x with the electron density n_e when (a) $T_e = 1$ keV and (b) $T_e = 5$ keV. The dot-dashed green (light gray) lines represent the upper and lower density boundaries of Region II when $T_e = 2.5$ keV.

transverse directions (y and z directions). This illustrates that the main acceleration mechanism is in the laser propagating direction (x direction), and the novel mechanism of electron acceleration by anti-Stokes Langmuir decay instability cascade of forward-SRS is the principal acceleration mechanism to generate hot electrons with energy above 100 keV in Region II.

V. DISCUSSION

The maximum momenta of electrons from three typical cases when $n_e = 0.1n_c$, $0.12n_c$, $0.2n_c$ in Region I, II, and III are shown in Fig. 3(a). As discussed above, when $n_e = 0.1n_c$ in Region I, the electrons are accelerated by backward-SRS, backward-SRS of forward-SRS and the Langmuir decay instability of rescattering to a maximum energy of nearly 820 keV. Then, when $n_e = 0.12n_c$ in Region II, the electrons are accelerated by backward-SRS and the ALDI2 of forward-SRS to a maximum energy of nearly 400 keV. Finally, when $n_e = 0.2n_c$ in Region III, the electrons are accelerated by backward-SRS and forward-SRS directly to a maximum energy of nearly 700 keV.

The ratios of electrons with energy above E_m^B in Region I and Region III are obviously higher than that in Region II (only ∼0.01% in Region II). These results illustrate that the optimal density region when $T_e = 2.5$ keV is $0.108n_c \lesssim n_e \lesssim 0.138n_c$ in Region II, in which the suprathermal electrons are reduced to a lower energy and lower ratio for indirect drive ICF experiments.

When the electron temperature varies, the upper and lower electron density boundaries of Region II also vary, as shown in Fig. 21. When $T_e = 1$ keV, the electron density range in Region II is $0.110n_c \lesssim n_e \lesssim 0.129n_c$ shown in Fig. 21(a). As

the temperature rises to $T_e = 2.5$ keV, the electron density is bounded in Region II between $0.108n_c \lesssim n_e \lesssim 0.138n_c$, as shown in Fig. 3(a), which is also marked in Figs. 21(a) and 21(b).

When the electron temperature rises still further to $T_e = 5$ keV, the electron density in Region II is bounded by $0.105n_c \lesssim n_e \lesssim 0.146n_c$, as shown in Fig. 21(b). That is to say, when T_e varies from 1 to 5 keV, which is the common electron temperature range in ICF experiments, the lower electron density boundary in Region II varies from $0.110n_c$ to $0.105n_c$ and the upper electron density boundary of Region II varies from $0.129n_c$ to $0.146n_c$.

This means that the boundaries of Region II change slightly when the electron temperature is in the range [1, 5] keV. Thus, our model for the electron density in Region II can be used to control the suprathermal electrons to be at a reduced level, since the suprathermal electrons are not sensitive to the electron temperature, as shown in Fig. 3(b). Since those Langmuir waves from backward-SRS and forward-SRS, however, saturate at a lower amplitude due to secondary [9,44], sideband-type instabilities [49,50], the model only gives an approximate lower limit of the threshold density for backward-SRS and forward-SRS coupling. That is, the model given in this paper predicts the safest region of electron density (Region II) to restrict the suprathermal electrons to be at a minimum level, where the two-stage electron acceleration process by backward-SRS and forward-SRS does not occur.

All of the calculations presented in this work assumed homogeneous plasma. However, the forward-SRS is very sensitive to the electron density inhomogeneity. Thus, when very localized homogeneity is possible, the convective gain of forward-SRS is enormous which may make the forward-SRS important in this local region. In the case of inhomogeneous plasma, an effective damping from density gradient exists such that the forward-SRS will be suppressed compared to that in homogeneous plasma. Therefore, it is likely that the two-stage acceleration of electrons by the backward-SRS and the forward-SRS will be much reduced in inhomogeneous plasma. We have conducted the simulations in inhomogeneous plasma with a density linearly increasing from $0.1n_c$ to $0.2n_c$, and found that the main mechanism of electron acceleration is the two-stage acceleration by backward-SRS and forward-SRS in high density region (such as $n_e = 0.2n_c$). In this particular inhomogeneous case, the spectra of backward-SRS and forward-SRS are broad with a large bandwidth. The ratio of hot electrons above 100 keV is less than that when $n_e = 0.2n_c$ in homogeneous plasma. More detailed studies are left for future research.

There are other possible mechanisms, such as Raman side-scatter and the two-plasmon decay instability which require at least two dimensions to stimulate, as the waves propagate sideways. In our 3D PIC simulations, the transverse dimensions of the simulation box were only $10\lambda_0 \times 10\lambda_0$, and the cell size in y and z was $\Delta y = \Delta z = \lambda_0$ due to the limitation of computing resources, therefore no transverse waves were resolved. We have also done the 2D simulations with enough precisions. Other parameters were the same as 1D or 3D PIC simulations, but the transverse dimension of the simulation box was $20\lambda_0$, and the cell size in y was $\Delta y = 0.1\lambda_0$. Because in our parameter regions from $0.1n_c$ to $0.2n_c$, the two-plasmon

decay instability is difficult to develop, which usually dominates near the quarter critical density. There indeed exists Raman side-scatter, which accelerates the electrons in both longitudinal and transverse directions. However, the dominant electron acceleration mechanisms are in the longitudinal direction by backward-SRS or forward-SRS or secondary instabilities.

Our work considers the effect of a single laser beam on energetic electron accelerations. In practice, a *Hohlraum* is not irradiated by a single laser beam but rather by several, each of moderate intensity, which cross the laser entrance hole at various angles, in a cone geometry. This cannot possibly be taken into account in our 1D and 3D simulations. This topic will be researched in the future. Thus, the study may be interesting as a means to produce fast electrons and hence hard x rays, or possibly for a fast ignition scheme.

In low-Z plasmas such as hydrogen (H), helium (He), or HeH(1:1), the collisional damping is much lower than the Landau damping, especially for the backward-SRS. Because in our simulations, the electron temperature is as high as $T_e = 2.5$ keV. The results from PIC simulations with collisional damping are nearly consistent to those from Vlasov simulations without collisional damping. However, in high-Z plasmas such as Au plasmas, the collisional damping is even stronger than the Landau damping of ion-acoustic waves. The research of parametric instabilities in different ion-species homogeneous [54] and inhomogeneous plasmas [53] were investigated in detail by Feng *et al.*

VI. CONCLUSION

In summary, a variety of different mechanisms in three distinct electron density regimes have been analyzed. A novel mechanism to accelerate electrons—anti-Stokes Langmuir decay instability cascade of forward-SRS—has been proposed to explain the generation of high-energy electrons in Region II, which cannot be explained by traditional mechanisms. The wave-breaking maximum electric field has been used to predict the necessary condition for the two-stage electron acceleration by backward-SRS and forward-SRS and to distinguish the regions within which different electron acceleration mechanisms are allowed. We have shown that in Region I, with density $n_e \lesssim 0.108n_c$, the rescattering and Langmuir decay instability of rescattering is an intermediate process which accelerates electrons trapped by the backward-SRS-induced Langmuir wave. In Region II, when the density is in the range $0.108n_c \lesssim n_e \lesssim 0.138n_c$, the ALDI2 (or second-stage anti-Stokes Langmuir decay instability cascade) of forward-SRS is the intermediate process that accelerates electrons trapped by the backward-SRS-induced Langmuir wave. Finally, in Region III, when $n_e \gtrsim 0.138n_c$, the two-stage electron acceleration process by backward-SRS and forward-SRS occurs.

When $T_e = 2.5$ keV, if $n_e > 0.138n_c$ (Region III), then $p^F_{\min} < p^B_{\max}$, and electrons trapped by the backward-SRS-induced Langmuir wave are further trapped and accelerated by the forward-SRS-induced Langmuir wave. This results in the generation of suprathermal electrons with energy higher than E^F_ϕ. As a result, one needs to reduce the electron density to be less than $n_e \sim 0.138n_c$ in indirect-drive ICF experiments to avoid suprathermal electron generation with energy higher than E^F_ϕ. From this work, within the density range $0.1n_c \leqslant n_e \leqslant 0.2n_c$, the better choice of the gas fill for *Hohlraum* targets in indirect-drive to suppress suprathermal electron generation is $0.108n_c \lesssim n_e \lesssim 0.138n_c$ (Region II). Beam smoothing techniques such as SSD [6] and PS [7] are well-known methods to reduce SBS and SRS, which will be included in the future studies.

It should be noted that the hot electron spectra and numbers via the anti-Stokes Langmuir decay instability cascade mechanism described here might be used as a method of inferring electron density information for the interior of *Hohlraum* targets for future indirect-drive experiments, since the suprathermal electrons that are generated are very sensitive to the precise electron density (of course, this information is limited by the electric fields associated with space charge separation which will also need to be accounted for).

Finally, the novel acceleration mechanism presented here offers a possible explanation for the source of the higher-energy electrons generation in indirect-drive experiments. Based on these mechanisms discussed here, it can promote the future mitigation strategies of hot electrons for experiments on the NIF. And it also provides a promising approach to accelerate the electrons to higher energy as a hard x-ray source for radiography purposes. Indeed, the use of plasma optics and beam-combiners [23,24] might aid this application. Future studies will also need to look at more precise requirements for the control of fast electron generation with the use of direct drive ICF, since suprathermal electron generation in the laser propagation direction during the compression phase is a critical parameter that must be controlled.

[1] C. S. Liu, M. N. Rosenbluth, and R. B. White, Phys. Fluids **17**, 1211 (1974).

[2] S. H. Glenzer, D. H. Froula, L. Divol, M. Dorr, R. L. Berger, S. Dixit, B. A. Hammel, C. Haynam, J. A. Hittinger, J. P.

Holder, O. S. Jones, D. H. Kalantar, O. L. Landen, A. B. Langdon, S. Langer, B. J. MacGowan, A. J. Mackinnon, N. Meezan, E. I. Moses, C. Niemann *et al.*, Nat. Phys. **3**, 716 (2007).

[3] S. H. Glenzer, B. J. MacGowan, P. Michel, N. B. Meezan, L. J. Suter, S. N. Dixit, J. L. Kline, G. A. Kyrala, D. K. Bradley, D. A. Callahan, E. L. Dewald, L. Divol, E. Dzenitis, M. J. Edwards, A. V. Hamza, C. A. Haynam, D. E. Hinkel, D. H. Kalantar, J. D. Kilkenny, O. L. Landen *et al.*, Science **327**, 1228 (2010).

[4] X. T. He, J. W. Li, Z. F. Fan, L. F. Wang, J. Liu, K. Lan, J. F. Wu, and W. H. Ye, Phys. Plasmas **23**, 082706 (2016).

[5] F. Zhang, H. B. Cai, W. M. Zhou, Z. S. Dai, L. Q. Shan, H. Xu, J. B. Chen, F. J. Ge, Q. Tang, W. S. Zhang, L. Wei, D. X. Liu, J. F. Gu, H. B. Du, B. Bi, S. Z. Wu, J. Li, F. Lu, H. Zhang, B. Zhang *et al.*, Nat. Phys. **16**, 810 (2020).

[6] S. Skupsky, R. W. Short, T. Kessler, R. S. Craxton, S. Letzring, and J. M. Soures, J. Appl. Phys. **66**, 3456 (1989).

[7] J. E. Rothenberg, J. Appl. Phys. **87**, 3654 (2000).

[8] G. Raj, B. Ersfeld, G. Vieux, S. Yoffe, M. S. Hur, R. A. Cairns, and D. A. Jaroszynski, New J. Phys. **17**, 103026 (2015).

[9] D. E. Hinkel, S. W. Haan, A. B. Langdon, T. R. Dittrich, C. H. Still, and M. M. Marinak, Phys. Plasmas **11**, 1128 (2004).

[10] A. B. Langdon and D. E. Hinkel, Phys. Rev. Lett. **89**, 015003 (2002).

[11] R. Yan, C. Ren, J. Li, A. V. Maximov, W. B. Mori, Z.-M. Sheng, and F. S. Tsung, Phys. Rev. Lett. **108**, 175002 (2012).

[12] K. Pan, S. Jiang, Q. Wang, L. Guo, S. Li, Z. Li, D. Yang, C. Zheng, B. Zhang, and X. He, Nucl. Fusion **58**, 096035 (2018).

[13] P. Bertrand, A. Ghizzo, S. J. Karttunen, T. J. H. Pättikangas, R. R. E. Salomaa, and M. Shoucri, Phys. Plasmas **2**, 3115 (1995).

[14] C. Rousseaux, F. Amiranoff, C. Labaune, and G. Matthieussent, Phys. Fluids B **4**, 2589 (1992).

[15] K. Estabrook, W. L. Kruer, and B. F. Lasinski, Phys. Rev. Lett. **45**, 1399 (1980).

[16] K. Estabrook and W. L. Kruer, Phys. Fluids **26**, 1892 (1983).

[17] B. J. Winjum, J. E. Fahlen, F. S. Tsung, and W. B. Mori, Phys. Rev. Lett. **110**, 165001 (2013).

[18] D. H. Froula, L. Divol, R. A. London, R. L. Berger, T. Döppner, N. B. Meezan, J. Ralph, J. S. Ross, L. J. Suter, and S. H. Glenzer, Phys. Plasmas **17**, 056302 (2010).

[19] R. K. Kirkwood, J. D. Moody, J. Kline, E. Dewald, S. Glenzer, L. Divol, P. Michel, D. Hinkel, R. Berger, E. Williams, J. Milovich, L. Yin, H. Rose, B. MacGowan, O. Landen, M. Rosen, and J. Lindl, Plasma Phys. Control. Fus. **55**, 103001 (2013).

[20] D. Hinkel, T. Döppner, L. Masse, K. Widmann, L. Divol, B. Bachmann, L. Berzak Hopkins, S. LePape, C. Weber, S. MacLaren, A. Zylstra, J. Ralph, L. Benedetti, A. Moore, C. Thomas, D. Casey, V. Smalyuk, H. Robey, P. Celliers, M. MacDonald *et al.*, High Energy Density Phys. **37**, 100884 (2020).

[21] T. Doppner, B. Bachmann, F. Albert, P. Bell, S. Burns, J. Celeste, R. Chow, L. Divol, E. L. Dewald, M. Hohenberger, N. Izumi, G. LaCaille, O. L. Landen, N. Palmer, H. S. Park, C. A. Thomas, and C. Huntington, J. Instrum. **11** (2016).

[22] M. Tabak, J. Hammer, M. E. Glinsky, W. L. Kruer, S. C. Wilks, J. Woodworth, E. M. Campbell, M. D. Perry, and R. J. Mason, Phys. Plasmas **1**, 1626 (1994).

[23] R. K. Kirkwood, D. P. Turnbull, T. Chapman, S. C. Wilks, M. D. Rosen, R. A. London, L. A. Pickworth, W. H. Dunlop, J. D. Moody, D. J. Strozzi, P. A. Michel, L. Divol, O. L. Landen, B. J. MacGowan, B. M. Van Wonterghem, K. B. Fournier, and B. E. Blue, Nat. Phys. **14**, 80 (2018).

[24] R. K. Kirkwood, D. P. Turnbull, T. Chapman, S. C. Wilks, M. D. Rosen, R. A. London, L. A. Pickworth, A. Colaitis, W. H. Dunlop, P. Poole, J. D. Moody, D. J. Strozzi, P. A. Michel, L. Divol, O. L. Landen, B. J. MacGowan, B. M. Van Wonterghem, K. B. Fournier, and B. E. Blue, Phys. Plasmas **25**, 056701 (2018).

[25] H. A. Makse, S. Havlin, and H. E. Stanley, Nature (Lond.) **377**, 608 (1995).

[26] N. Lemos, P. King, J. L. Shaw, A. L. Milder, K. A. Marsh, A. Pak, B. B. Pollock, C. Goyon, W. Schumaker, A. M. Saunders, D. Papp, R. Polanek, J. E. Ralph, J. Park, R. Tommasini, G. J. Williams, H. Chen, F. V. Hartemann, S. Q. Wu, S. H. Glenzer *et al.*, Phys. Plasmas **26**, 083110 (2019).

[27] J. L. Kline, D. S. Montgomery, B. Bezzerides, J. A. Cobble, D. F. DuBois, R. P. Johnson, H. A. Rose, L. Yin, and H. X. Vu, Phys. Rev. Lett. **94**, 175003 (2005).

[28] J. L. Kline, D. S. Montgomery, L. Yin, D. F. DuBois, B. J. Albright, B. Bezzerides, J. A. Cobble, E. S. Dodd, D. F. DuBois, J. C. Fernández, R. P. Johnson, J. M. Kindel, H. A. Rose, H. X. Vu, and W. Daughton, Phys. Plasmas **13**, 055906 (2006).

[29] D. W. Forslund, J. M. Kindel, and E. L. Lindman, Phys. Fluids **18**, 1002 (1975).

[30] R. L. Berger, C. H. Still, E. A. Williams, and A. B. Langdon, Phys. Plasmas **5**, 4337 (1998).

[31] L. Hao, Z. Liu, C. Zheng, J. Xiang, W. Feng, X. Hu, and B. Li, Chin. Sci. Bull. **57**, 2747 (2012).

[32] D. F. DuBois, D. W. Forslund, and E. A. Williams, Phys. Rev. Lett. **33**, 1013 (1974).

[33] R. L. Berger, L. J. Suter, L. Divol, R. A. London, T. Chapman, D. H. Froula, N. B. Meezan, P. Neumayer, and S. H. Glenzer, Phys. Rev. E **91**, 031103(R) (2015).

[34] J. D. Lindl, P. Amendt, R. L. Berger, S. G. Glendinning, S. H. Glenzer, S. W. Haan, R. L. Kauffman, O. L. Landen, and L. J. Suter, Phys. Plasmas **11**, 339 (2004).

[35] D. J. Strozzi, PhD thesis, Physics Department, Massachusetts Institute of Technology (2005), p. 42.

[36] W. B. Mori and T. Katsouleas, Phys. Scr. **1990**, 127 (1990).

[37] E. Esarey, C. B. Schroeder, and W. P. Leemans, Rev. Mod. Phys. **81**, 1229 (2009).

[38] T. P. Coffey, Phys. Fluids **14** (1971).

[39] T. Katsouleas and W. B. Mori, Phys. Rev. Lett. **61**, 90 (1988).

[40] R. M. G. M. Trines and P. A. Norreys, Phys. Plasmas **13**, 123102 (2006).

[41] Z. J. Liu, S. P. Zhu, L. H. Cao, C. Y. Zheng, X. T. He, and Y. Wang, Phys. Plasmas **16**, 112703 (2009).

[42] Q. Wang, Z. J. Liu, C. Y. Zheng, C. Z. Xiao, Q. S. Feng, H. C. Zhang, and X. T. He, Phys. Plasmas **25**, 012708 (2018).

[43] Q. S. Feng, Z. J. Liu, C. Y. Zheng, C. Z. Xiao, Q. Wang, H. C. Zhang, L. H. Cao, and X. T. He, Plasma Phys. Control. Fus. **59**, 075007 (2017).

[44] Q. S. Feng, C. Y. Zheng, Z. J. Liu, L. H. Cao, Q. Wang, C. Z. Xiao, and X. T. He, Phys. Plasmas **25**, 092112 (2018).

[45] Q. Feng, L. Cao, Z. Liu, C. Zheng, and X. He, Sci. Rep. **10**, 3492 (2020).

[46] J. Bergman and B. Eliasson, Phys. Plasmas **8**, 1482 (2001).

[47] L. Yin, W. Daughton, B. J. Albright, K. J. Bowers, D. S. Montgomery, J. L. Kline, J. C. Fernández, and Q. Roper, Phys. Plasmas **13**, 072701 (2006).

[48] S. J. Karttunen, Phys. Rev. A **23**, 2006 (1981).

[49] S. Brunner and E. J. Valeo, Phys. Rev. Lett. **93**, 145003 (2004).

[50] S. Brunner, R. L. Berger, B. I. Cohen, L. Hausammann, and E. J. Valeo, Phys. Plasmas **21**, 102104 (2014).

[51] D. S. Montgomery, R. J. Focia, H. A. Rose, D. A. Russell, J. A. Cobble, J. C. Fernández, and R. P. Johnson, Phys. Rev. Lett. **87**, 155001 (2001).

[52] T. D. Arber, K. Bennett, C. S. Brady, A. Lawrence-Douglas, M. G. Ramsay, N. J. Sircombe, P. Gillies, R. G. Evans, H. Schmitz, A. R. Bell, and C. P. Ridgers, Plasma Phys. Control. Fusion **57**, 113001 (2015).

[53] Q. Feng, Z. Liu, L. Cao, C. Xiao, L. Hao, C. Zheng, C. Ning, and X. He, Nucl. Fusion **60**, 066012 (2020).

[54] Q. S. Feng, C. Y. Zheng, Z. J. Liu, L. H. Cao, Q. Wang, C. Z. Xiao, and X. T. He, Phys. Plasmas **26**, 052101 (2019).